Available online at www.sciencedirect.com
ScienceDirect
Comput. Methods Appl. Mech. Engrg. 385 (2021) 114014
Computer methods in applied mechanics and engineering
www.elsevier.com/locate/cma

Stochastic modeling of geometrical uncertainties on complex domains, with application to additive manufacturing and brain interface geometries

Hao Zhang[a], Johann Guilleminot[a,*], Luis J. Gomez[b]

[a] *Department of Civil and Environmental Engineering, Duke University, NC, 27708, USA*
[b] *Department of Electrical and Computer Engineering, Purdue University, IN, 47907, USA*

Received 7 December 2020; received in revised form 2 April 2021; accepted 18 June 2021
Available online xxxx

Abstract

We present a stochastic modeling framework to represent and simulate spatially-dependent geometrical uncertainties on complex geometries. While the consideration of random geometrical perturbations has long been a subject of interest in computational engineering, most studies proposed so far have addressed the case of regular geometries such as cylinders and plates. Here, standard random field representations, such as Karhunen–Loève expansions, can readily be used owing, in particular, to the relative simplicity to construct covariance operators on regular shapes. On the contrary, applying such techniques on arbitrary, non-convex domains remains difficult in general. In this work, we formulate a new representation for spatially-correlated geometrical uncertainties that allows complex domains to be efficiently handled. Building on previous contributions by the authors, the approach relies on the combination of a stochastic partial differential equation approach, introduced to capture salient features of the underlying geometry such as local curvature and singularities on the fly, and an information-theoretic model, aimed to enforce non-Gaussianity. More specifically, we propose a methodology where the interface of interest is immersed into a fictitious domain, and define algorithmic procedures to directly sample random perturbations on the manifold. A simple strategy based on statistical conditioning is also presented to update realizations and prevent self-intersections in the perturbed finite element mesh. We finally provide challenging examples to demonstrate the robustness of the framework, including the case of a gyroid structure produced by additive manufacturing and brain interfaces in patient-specific geometries. In both applications, we discuss suitable parameterization for the filtering operator and quantify the impact of the uncertainties through forward propagation.

Keywords: Imperfections; Geometrical uncertainties; Random field; Uncertainty quantification

1. Introduction

Random geometrical uncertainties are ubiquitous in many engineering applications. Evidence of so-called random imperfections and their effects on system performance can be found in a broad array of fields, ranging from contact mechanics and tribology [1], to buckling of nanocomposite structures [2,3], to the design of origami-based

* Corresponding author.
E-mail address: johann.guilleminot@duke.edu (J. Guilleminot).

https://doi.org/10.1016/j.cma.2021.114014

metamaterials [4–6]. Examples can also be found in [7,8] for parts produced by additive manufacturing, in [9–16] for the analysis of cylindrical shells under geometrical imperfections, as well as in [2,3,17–27] for composite structures under various types of loading conditions—to list a few. The existence of such imperfections is often attributed to the underlying manufacturing technology, which inevitably introduces deviations from nominal models due to, e.g., precision limitations (see [28,29] for additive manufacturing techniques), as well as to service conditions. Another potential source of geometrical uncertainties lies into data acquisition chains where raw data sets can be corrupted by post-processing steps. Segmentation in digital image analysis is one relevant example where low contrasts, combined with geometrical complexity, can lead to substantial errors in classification.

In this context, uncertainty quantification techniques have been extensively deployed to investigate the impact of geometrical uncertainties on quantities of interest (such as buckling loads for composite shells, or foldability for origami-type structures; see the aforementioned references), with the aim of better understanding and mitigating system variability. These uncertainties are often modeled as spatially-dependent random parameters and thus, a random field representation must be adopted. A natural way to construct such a representation relies on the definition of a Gaussian model (which is assumed centered without loss of generality) that can eventually be pushed forward to obtain a non-Gaussian model, depending on the retained state space. Regardless of the latter, the consideration of an underlying Gaussian model facilitates the sampling task, as generation techniques for such fields are numerous and well proven (including spectral methods [30,31], factorization techniques [32–38], and Karhunen–Loève expansions [39–41]). In addition, the combination of a Gaussian model and a transport map leads to a low-dimensional parameterization of the resulting non-Gaussian model (that is, the number of hyperparameters in the stochastic model is small) that is more appropriate for inverse identification than more general representations such as polynomial chaos expansions of random fields. From a stochastic modeling standpoint, the methodology requires the construction of a covariance function (for the Gaussian model) describing how the uncertainties are correlated with one another over the domain of interest. For stationary fields indexed on regular geometries such as cylinders, plates, and spheres, covariance functions are usually quite easy to define in closed-form. However, this central task becomes more challenging on complex index sets presenting curved, non-convex features and topological singularities. While standard models can readily be extended to tackle such problems using a parameterization based on a geodesic distance (see, e.g., [42]), their use is practically limited to the case of isotropic correlation structures.

In this work, we formulate an ad hoc random field representation that allows complex domains to be efficiently handled. The methodology builds on the combination of a stochastic partial differential equation approach (SPDE), introduced to capture the salient features of the geometry such as local curvature, non-convexity, and topological singularities, in the definition of the underlying Gaussian random field (which can exhibit an isotropic or an anisotropic correlation structure), and an information-theoretic model, aimed to enforce boundedness on perturbations and hence, non-Gaussianity. This contribution differs from previous works by the authors, which were primarily focused on stochastic constitutive models [43–45], in that the random field is here defined and directly sampled on a manifold. To address this situation, we present new methodological developments adapted to the modeling of spatially-correlated geometrical uncertainties. More specifically, we first introduce a strategy where the interface of interest is immersed into a fictitious domain in $\mathbb{R}^d$. The coefficient in the SPDE filtering operator is then conveniently defined by projecting the gradients of the solutions to (still) fictitious Laplace problems onto the interface. Second, we construct an appropriate algebraic representation and derive a push-forward transport map that ensures well-posedness and provides reasonable modeling flexibility. Third, we propose a simple updating procedure to tackle conflicting perturbations, which result in local self-intersection in the finite element mesh, at a reasonable computational cost using conditional sampling. In order to demonstrate the robustness of the framework, we finally report numerical results pertaining to the modeling and sampling of correlated stochastic perturbations on surfaces with increasing levels of complexity, including the case of a highly porous structure and brain interfaces in patient-specific geometries. In particular, we discuss the parameterization of the stochastic model accounting for both the nominal geometrical model and the process at the origin of the uncertainties.

The rest of this paper is organized as follows. The stochastic model and methodological aspects are first presented in Section 2. We introduce, in particular, the random field representation for geometrical uncertainties, including the stochastic partial differential equation approach, the updating procedure, and the information-theoretic probabilistic model. Numerical applications are then provided and used to analyze the performance of the framework in Section 3. Conclusions are finally drawn in Section 4.

2. Stochastic modeling framework

2.1. Overview of the methodology

Let Ω be a connected, bounded and open domain in $\mathbb{R}^d$ with piecewise smooth boundary Γ. A natural way to define a random perturbation $\widetilde{\Gamma}$ of Γ is to construct a stochastic mapping $\boldsymbol{x}_\Gamma \mapsto \boldsymbol{X}_{\widetilde{\Gamma}}(\boldsymbol{x}_\Gamma)$, where positions $\boldsymbol{x}_\Gamma \in \Gamma$ are each assigned a random variable $\boldsymbol{X}_{\widetilde{\Gamma}}(\boldsymbol{x}_\Gamma)$ defined on a probability space $(\Theta, \mathcal{F}, \mathcal{P})$. In this setting, the family $\{\boldsymbol{X}_{\widetilde{\Gamma}}(\boldsymbol{x}_\Gamma), \boldsymbol{x}_\Gamma \in \Gamma\}$ can be interpreted as a random field. For a fixed $\theta \in \Theta$, we denote by $\widetilde{\Gamma}(\theta)$ the realization containing the set of points $\{\boldsymbol{X}_{\widetilde{\Gamma}}(\boldsymbol{x}_\Gamma, \theta), \boldsymbol{x}_\Gamma \in \Gamma\}$, hence defining a realization of the randomly perturbed manifold $\widetilde{\Gamma}$. Here, we consider a stochastic mapping defined by the additive decomposition

$$\boldsymbol{X}_{\widetilde{\Gamma}}(\boldsymbol{x}_\Gamma) := \boldsymbol{x}_\Gamma + (\zeta(\boldsymbol{x}_\Gamma) + \eta)\boldsymbol{d}_\Gamma(\boldsymbol{x}_\Gamma) \ , \quad \forall \boldsymbol{x}_\Gamma \in \Gamma \ , \tag{1}$$

where $\zeta(\boldsymbol{x}_\Gamma)$ and η are random variables to be defined momentarily, and $\boldsymbol{d}_\Gamma(\boldsymbol{x}_\Gamma)$ is a unit vector indicating the direction of the perturbation at point $\boldsymbol{x}_\Gamma$. In Eq. (1), η is used to represent random homogeneous perturbations, if any, while the random field $\{\zeta(\boldsymbol{x}_\Gamma), \boldsymbol{x}_\Gamma \in \Gamma\}$ is introduced to model random spatially-correlated perturbations. The system of marginal distributions of $\widetilde{\Gamma}$ is thus determined by the probabilistic models for the random field $\{\zeta(\boldsymbol{x}_\Gamma), \boldsymbol{x}_\Gamma \in \Gamma\}$ and random variable η, as well as by the choice of the direction field $\boldsymbol{d}_\Gamma$. These models and the associated parameters must be carefully chosen to accurately represent the uncertainty of the underlying physical geometry. For the applications considered here, $\{\zeta(\boldsymbol{x}_\Gamma), \boldsymbol{x}_\Gamma \in \Gamma\}$ and η must take values in bounded subsets of $\mathbb{R}$, which are denoted by $\mathcal{S}_\zeta$ and $\mathcal{S}_\eta$ respectively, because the magnitude of the geometrical perturbations is assumed to be bounded from above and below almost surely (that is, with probability 1). The construction of a probabilistic model for η is standard in the literature of uncertainty quantification and is not addressed hereinafter (see Section 3.2 for an example). The task of constructing a model for the random field $\{\zeta(\boldsymbol{x}_\Gamma), \boldsymbol{x}_\Gamma \in \Gamma\}$ is more intricate when Γ is not a simple manifold (e.g., the surface of a sphere or a cylinder for $d = 3$) on which probabilistic properties can intuitively be described. In order to address this challenge, we proceed following a two-step methodology. A real-valued and normalized Gaussian random field, denoted by $\{\Xi(\boldsymbol{x}_\Gamma), \boldsymbol{x}_\Gamma \in \Gamma\}$, is first defined and set to capture the geometrical structure of Γ. Then, a transport map T is used to push forward the system of first-order marginal distributions to a system of distributions having support $\mathcal{S}_\zeta$:

$$\zeta(\boldsymbol{x}_\Gamma) = T(\Xi(\boldsymbol{x}_\Gamma)) \ , \quad \forall \boldsymbol{x}_\Gamma \in \Gamma \ . \tag{2}$$

Although not explored here, the mapping T can be made spatially dependent to introduce nonstationary effects in the system of first-order marginal distributions. It should be noticed that the correlation function of $\{\Xi(\boldsymbol{x}_\Gamma), \boldsymbol{x}_\Gamma \in \Gamma\}$ and the map T implicitly define the entire system of marginal distributions for the random field $\{\zeta(\boldsymbol{x}_\Gamma), \boldsymbol{x}_\Gamma \in \Gamma\}$. The above construction ensures the admissibility and geometrical consistency of the realizations for the perturbed manifold $\widetilde{\Gamma}$.

The definition of stochastic models for the underlying Gaussian field and the transport map is discussed in the rest of this section. Specifically, Section 2.2 both defines the Gaussian random field and provides the computational method that is used to sample it. In Section 2.3, we present a methodology to handle locally-conflicting perturbations. Section 2.4 is devoted to the construction of the transport map T.

2.2. Construction of the underlying Gaussian random field

2.2.1. Definition in the bounded domain $\Omega \subset \mathbb{R}^d$

Before proceeding with the methodology to define and sample normalized Gaussian random fields on the manifold Γ, this section details necessary background pertaining to the Matérn class of Gaussian random fields indexed by $\Omega \subset \mathbb{R}^d$. This class of Gaussian fields is considered in this paper due to its relevance in probabilistic modeling for spatially-correlated uncertainties; see, e.g., [46] for a discussion in the context of Bayesian inference, as well as the references cited at the end of this section. Perhaps more importantly, elements in that class also admit an implicit representation that can be leveraged to conveniently accommodate complex index sets through a proper geometry-informed parameterization—as discussed in subsequent sections; see Sections 2.2.2 and 2.2.3 in particular.

Let $\mathbb{E}$ denote the operator of mathematical expectation. An isotropic centered stationary Gaussian random field $\{U(\boldsymbol{x}), \boldsymbol{x} \in \mathbb{R}^d\}$ is said to be of Matérn type if its covariance function $(\boldsymbol{x}, \boldsymbol{y}) \mapsto C(\boldsymbol{x}, \boldsymbol{y}) = \mathbb{E}(U(\boldsymbol{x})U(\boldsymbol{y}))$ is defined as

$$C(\boldsymbol{x}, \boldsymbol{y}) = \sigma^2 \frac{2^{1-\nu}}{\mathbb{G}(\nu)} \left(\kappa \|\boldsymbol{x} - \boldsymbol{y}\|\right)^{\nu} K_{\nu} \left(\kappa \|\boldsymbol{x} - \boldsymbol{y}\|\right) \ , \quad \forall \boldsymbol{x}, \boldsymbol{y} \in \mathbb{R}^d \ , \tag{3}$$

where $\|\cdot\|$ is the Euclidean norm in $\mathbb{R}^d$, σ^2 is the marginal variance of the field, $\mathbb{G}$ is the Gamma function, $\kappa > 0$ and $\nu > 0$ are the scale and smoothness parameters, and K_ν is the modified Bessel function of the second kind (of order ν); see [47], p. 18. The parameter $(1/\kappa)$ is often interpreted as a correlation range parameter, while ν defines the mean-square differentiability of the field. For $\nu = 1/2$ and $\nu \to +\infty$, the Matérn covariance function reduces to the standard exponential and squared exponential covariance functions, respectively.

It was shown by Whittle that a Matérn-type Gaussian random field in $\mathbb{R}^d$ can be defined as the stationary solution to the following fractional stochastic partial differential equation (SPDE):

$$(\kappa^2 \mathcal{I} - \Delta)^{\alpha/2} U = \dot{W} \ , \tag{4}$$

where $\mathcal{I}$ and Δ are the identity and Laplacian operators, $\alpha = (\nu + d/2)$, $\dot{W}$ denotes the normalized Gaussian white noise in $\mathbb{R}^d$, and equality holds in the sense of distributions [48]. In this case, the conditional variance σ^2 in Eq. (3) is given by

$$\sigma^2 = \frac{\mathbb{G}(\nu)}{\mathbb{G}(\nu + d/2)(4\pi)^{d/2}\kappa^{2\nu}} \ . \tag{5}$$

The driving term in Eq. (4) can be scaled to define a Gaussian field $\{U(\boldsymbol{x}), \boldsymbol{x} \in \mathbb{R}^d\}$ with unit pointwise variance (as specified in the methodology introduced in Section 2.1). Proceeding with the change of variable $\ell := 1/\kappa$, we obtain the SPDE

$$(\mathcal{I} - \ell^2 \Delta)^{\alpha/2} U = \phi \dot{W} \ , \tag{6}$$

in which ϕ is defined as

$$\phi^2 := \frac{\mathbb{G}(\nu + d/2)(4\pi)^{d/2}}{\mathbb{G}(\nu)\kappa^d} = \frac{\mathbb{G}(\nu + d/2)(4\pi)^{d/2}\ell^d}{\mathbb{G}(\nu)} \ . \tag{7}$$

The above interpretation has recently regained popularity following the seminal work [49] where the authors proposed a computationally efficient way to solve the SPDE, supplemented with homogeneous Neumann boundary conditions, on bounded domains. Specifically, by introducing the finite-dimensional representation

$$U(\boldsymbol{x}) = \sum_{i=1}^{n} U_i \psi_i(\boldsymbol{x}) \ , \quad \boldsymbol{x} \in \Omega \ , \tag{8}$$

where $\{U_i\}_{i=1}^n$ is a set of random variables and $\{\psi_i\}_{i=1}^n$ are piecewise linear basis functions defined on a n-node mesh of Ω, it was shown that the weak Galerkin stochastic solution (defined for $\alpha = 2$) satisfies

$$\boldsymbol{U} \sim \mathcal{N}(\boldsymbol{0}, [Q]^{-1}) \ , \tag{9}$$

in which $\boldsymbol{U} = (U_1, \ldots, U_n)^{\mathsf{T}}$ is the random vector of stochastic nodal values, $\mathcal{N}$ denotes the normal distribution, and the precision matrix $[Q]$ is given by

$$[Q] = \frac{1}{\phi^2}([M] + \ell^2[G])[M]^{-1}([M] + \ell^2[G]) \ , \tag{10}$$

with $M_{ij} = \langle \psi_i, \psi_j \rangle_\Omega$, $G_{ij} = \langle \nabla\psi_i, \nabla\psi_j \rangle_\Omega$, and $\langle f, g \rangle_\Omega := \int_\Omega \langle f(\boldsymbol{x}), g(\boldsymbol{x}) \rangle \, \mathrm{d}\boldsymbol{x}$ is the standard inner product between vector-valued functions in $\mathbb{R}^d$. Notice that the precision matrix and the associated solution for arbitrary (integer) orders can be obtained using a recursive formula (see [49]). In practice, $[Q]$ is easily obtained by means of a finite element assembly procedure, and realizations of $\boldsymbol{U}$ can then be generated by using an appropriate sampling technique, such as direct or iterative factorization methods.

Following [50], Gaussian random fields with anisotropic covariance functions can be defined in $\mathbb{R}^d$ as the solution to the SPDE

$$(\kappa^2 \mathcal{I} - \langle \nabla, [H]\nabla \rangle)^{\alpha/2} U = \dot{W} \ , \tag{11}$$

where $[H]$ denotes a spatially-varying field with values in the set $\mathbb{S}^d_{>0}$ of $(d \times d)$ symmetric positive definite matrices, termed the diffusion field; see [51–53] for studies with a constant diffusion field. In this case, the precision matrix $[Q]$ is still defined according to Eq. (10), in which the entries in the mass and stiffness matrices are given by $M_{ij} = \langle \psi_i, \psi_j \rangle_\Omega$ and $G_{ij} = \langle \nabla\psi_i, [H]\nabla\psi_j \rangle_\Omega$, respectively. The definition of H is a modeling issue and remains application-dependent. To enable physical interpretation, one shall assume a simple parameterization of the form

$$[H(\boldsymbol{x})] = \sum_{i=1}^{d} \lambda_i \boldsymbol{e}^i(\boldsymbol{x}) \otimes \boldsymbol{e}^i(\boldsymbol{x}) \ , \quad \forall \boldsymbol{x} \in \Omega \ , \tag{12}$$

where $\{\boldsymbol{e}^i\}_{i=1}^d$ are fields of unit orientation vectors governing the directions of white noise local filtering and $\{\lambda_i\}_{i=1}^d$ are strictly positive parameters controlling correlation ranges along these directions.

Examples of applications for the above framework include Bayesian inference [28,52–56], climate modeling [57], and stochastic modeling and simulations in computational mechanics [43–45,58] (to list a few). Various extensions were also proposed, addressing the integration of anisotropic and nonstationary features [50], the generalization to other classes of covariance functions [57], and the consideration of arbitrary smoothness parameters [59] or non-Gaussian driving terms [60]. It should be noticed that suitable boundary conditions must be chosen to avoid spurious folding-type effects on bounded domains. In order to address this issue, other types of boundary conditions were studied in [51,52,61]. It was shown, in particular, that appropriate tuning in Robin conditions delivers more accurate results in terms of both pointwise variance and covariance function than Dirichlet and Neumann boundary conditions.

2.2.2. *Defining and sampling random fields with isotropic covariance structures on Γ*

We now turn to the modeling and sampling of the underlying Gaussian field on the boundary Γ of $\Omega \subset \mathbb{R}^d$, which constitutes a $(d-1)$-dimensional manifold. It is below assumed that Γ is either closed or has boundaries that themselves constitute piecewise smooth $(d-2)$-dimensional manifolds. In this case, the theoretical framework presented in Section 2.2.1 can be readily used (see Appendix B in [49] for theoretical analysis) to define the random field indexed by Γ, owing to the use of the inner product

$$\langle f, g \rangle_\Gamma := \int_{\boldsymbol{x} \in \Gamma} \langle f(\boldsymbol{x}), g(\boldsymbol{x}) \rangle \, H^{d-1}_\Gamma(\mathrm{d}\boldsymbol{x}) \ , \tag{13}$$

where $H^{d-1}_\Gamma(A)$ denotes the Hausdorff measure of A; see [62] for mathematical details. In order to solve the SPDE using the Galerkin approach ($\alpha = 2$), we approximate the boundary Γ with a conforming triangulation $\mathcal{T}_h$ (note that the dependence on h is omitted from now on to simplify notation) and expand the underlying Gaussian random field (defining the seed for the spatially-correlated uncertainties) as

$$\Xi(\boldsymbol{x}_\Gamma) = \sum_{i=1}^{n_\Gamma} \Xi_i \varphi_i(\boldsymbol{x}_\Gamma) \ , \quad \forall \boldsymbol{x}_\Gamma \in \mathcal{T}_h \ , \tag{14}$$

where $\{\varphi_i\}_{i=1}^{n_\Gamma}$ are shape functions on $\mathcal{T}_h$. The random vector of coefficients $\boldsymbol{\Xi} = (\Xi_1, \ldots, \Xi_{n_\Gamma})^\mathsf{T}$ is then distributed according to $\boldsymbol{\Xi} \sim \mathcal{N}(\boldsymbol{0}, [Q]^{-1})$, where the precision matrix $[Q]$ is defined as in Section 2.2.1 with $M_{ij} = \langle \varphi_i, \varphi_j \rangle_\Gamma$ and $G_{ij} = \langle \nabla\varphi_i, \nabla\varphi_j \rangle_\Gamma$. These matrices $[M]$ and $[G]$ involve integrals that can be evaluated with the Lebesgue measure on the triangulated interface, given that the Hausdorff measure is, in practice, evaluated on the canonical Euclidean space with the Euclidean metric. In order to evaluate these integrals, the so-called mapping method presented in [63] is employed in this work. Here, a map $(\xi_1, \xi_2) \mapsto (x_1, x_2, x_3)$ is defined on each element $\mathcal{T}_e$ of $\mathcal{T}_h$, where (ξ_1, ξ_2) denotes the pair of coordinates in the parent element $\widehat{\mathcal{T}}$, embedded in $\mathbb{R}^2$, and (x_1, x_2, x_3) is the triplet of coordinates in the physical element $\mathcal{T}_e$ in $\mathbb{R}^3$. Hence, coordinates in the physical element are mapped as $\boldsymbol{x} = \sum_i \boldsymbol{x}^{(i)} \psi_i(\xi_1, \xi_2)$, where $\{\boldsymbol{x}^{(i)}\}_i$ are vectors of physical coordinates in $\mathbb{R}^3$ and $\{\psi_i\}_i$ are shape functions on the parent element. The physical derivatives on the surface can then be written as

$$\begin{bmatrix} \frac{\partial}{\partial x_1} \\ \frac{\partial}{\partial x_2} \\ \frac{\partial}{\partial x_3} \end{bmatrix} = [J]^{-1} \begin{bmatrix} \frac{\partial}{\partial \xi_1} \\ \frac{\partial}{\partial \xi_2} \\ 0 \end{bmatrix} \ , \quad [J] = \begin{bmatrix} \frac{\partial x_1}{\partial \xi_1} & \frac{\partial x_2}{\partial \xi_1} & \frac{\partial x_3}{\partial \xi_1} \\ \frac{\partial x_1}{\partial \xi_2} & \frac{\partial x_2}{\partial \xi_2} & \frac{\partial x_3}{\partial \xi_2} \\ n_1 & n_2 & n_3 \end{bmatrix} \ , \tag{15}$$

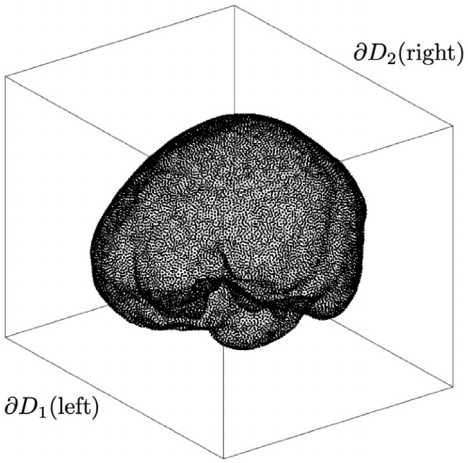

Fig. 1. Example of domain immersion. Here, Ω corresponds to a domain whose boundary is defined by the interface between the bone and the cerebrospinal fluid in a patient-specific brain geometry, and the domain is immersed into a cubic box D. The boundaries ∂D_1 and ∂D_2 correspond to the left and right external faces of ∂D, respectively.

where $[J]$ denotes the Jacobian matrix and $\boldsymbol{n} = (n_1, n_2, n_3)^{\mathsf{T}}$ denotes the outward pointing unit vector normal to the triangular facet at the point under consideration in $\mathbb{R}^3$. Using an isoparametric formulation, the matrices $[M]$ and $[G]$ can subsequently be evaluated in the parent domain, similarly to finite element matrices. A key observation is that the description of the interface Γ is implicitly encoded in the mapping method, through the field $\boldsymbol{x}_\Gamma \mapsto \boldsymbol{n}(\boldsymbol{x}_\Gamma)$ of outward pointing normal vectors.

As previously indicated, realizations of the stochastic field (at the nodes of the triangulation) can readily be computed using standard techniques, such as direct or iterative factorization methods, once $[Q]$ has been assembled. In this work, we use a Cholesky factorization technique: a sample $\boldsymbol{u}(\theta)$ of $\boldsymbol{U}$ is thus obtained by solving the linear system $[R]\boldsymbol{u}(\theta) = \boldsymbol{w}(\theta)$, where $[R]$ is the upper triangular matrix corresponding to the Cholesky decomposition of the precision matrix $[Q]$, and $\boldsymbol{w}(\theta)$ is a sample of $\boldsymbol{W} \sim \mathcal{N}(\boldsymbol{0}, [I_n])$ (with $[I_n]$ the $n \times n$ identity matrix).

2.2.3. Defining and sampling random fields with anisotropic covariance structures on Γ

The formulation presented in Section 2.2.2 leads to locally isotropic covariance structures. In this section, we address the case of anisotropic covariance structures on Γ, including user-specified principal directions and orientation-dependent correlation ranges. This setting necessitates the development of an appropriate methodology to define the diffusion field $\boldsymbol{x}_\Gamma \mapsto [H(\boldsymbol{x}_\Gamma)]$, which now takes values in the set $\mathbb{S}^{d-1}_{\succ 0}$.

For geometries presenting some symmetries, one possible approach consists in immersing the domain Ω into a regularly shaped, open bounded domain C and in defining the orientation fields using fictitious potential flow problems defined over $D := C \setminus \Omega$. In order to illustrate this approach, let us consider the case $\Omega \subset \mathbb{R}^3$ (Γ is thus a closed surface) and a parallelepiped domain $C \subset \mathbb{R}^3$. Let ∂D be the boundary of D, which is the union of the boundary ∂C of C and the interface of interest Γ. External faces $\{\partial D_k\}_{k=1}^6$ (such that $\partial D_k \cap \Gamma = \emptyset, \forall k$) are labeled such that ∂D_{2i-1} and ∂D_{2i}, $i \in \{1, 2, 3\}$, represent opposite faces (see Fig. 1 for an example). A fictitious Laplace problem is then introduced as

$$\Delta \Psi(\boldsymbol{x}) = 0 \ , \quad \forall \boldsymbol{x} \in D \ , \tag{16}$$

and is supplemented with Dirichlet boundary conditions at selected external faces

$$\begin{cases} \Psi(\boldsymbol{x}) = 0 \ , & \forall \boldsymbol{x} \in \partial D_{2i-1} \ , \\ \Psi(\boldsymbol{x}) = 1 \ , & \forall \boldsymbol{x} \in \partial D_{2i} \ , \end{cases} \tag{17}$$

and with Neumann boundary conditions

$$\langle \nabla \Psi(\boldsymbol{x}), \boldsymbol{n}(\boldsymbol{x}) \rangle = 0 \ , \quad \forall \boldsymbol{x} \in \partial D \setminus (\partial D_{2i-1} \cup \partial D_{2i}) \ , \tag{18}$$

where $\boldsymbol{n}(\boldsymbol{x})$ denotes the outward normal unit vector at location $\boldsymbol{x}$ on the boundary. Let Ψ_1 and Ψ_2 be the two solution fields obtained by solving the Laplace problem above with Dirichlet boundary conditions (see Eq. (17)) applied on two different sets of faces, e.g., ∂D_1 and ∂D_2 for the first Laplace problem, and ∂D_3 and ∂D_4 for the second Laplace problem. Let $\{\boldsymbol{v}^i\}_{i=1}^2$ denote the associated velocity flows:

$$\boldsymbol{v}^i(\boldsymbol{x}) = \nabla \Psi_i(\boldsymbol{x}) \ , \quad \forall \boldsymbol{x} \in D \ , \quad i \in \{1,2\} \ . \tag{19}$$

The orientation fields on the triangulated surface Γ_h are finally defined by normalizing the projections of the velocity flows onto Γ_h:

$$\boldsymbol{e}^i(\boldsymbol{x}_\Gamma) = \frac{1}{\|\boldsymbol{v}^i_{\Gamma_h}(\boldsymbol{x}_\Gamma)\|} \boldsymbol{v}^i_{\Gamma_h}(\boldsymbol{x}_\Gamma) \ , \quad \forall \boldsymbol{x}_\Gamma \in \Gamma \ , \quad i \in \{1,2\} \ , \tag{20}$$

where $\boldsymbol{v}^i_{\Gamma_h}$ denotes the projection of $\boldsymbol{v}^i$ onto Γ_h, computed with a nearest-point search in the neighborhood of $\boldsymbol{x}_\Gamma$. The diffusion field $[H]$ is then defined as

$$[H(\boldsymbol{x}_\Gamma)] = \sum_{i=1}^{2} \lambda_i \boldsymbol{e}^i(\boldsymbol{x}_\Gamma) \otimes \boldsymbol{e}^i(\boldsymbol{x}_\Gamma) \ , \quad \forall \boldsymbol{x}_\Gamma \in \Gamma \ , \tag{21}$$

and the entries of the system matrices $[M]$ and $[G]$ are computed for $\alpha = 2$ as $M_{ij} = \langle \psi_i, \psi_j \rangle_\Gamma$ and $G_{ij} = \langle \nabla\psi_i, [H]\nabla\psi_j \rangle_\Gamma$. The precision matrix $[Q]$ can then be evaluated using Eq. (10). Applications of this formulation are provided in Sections 3.1 and 3.2.

Remark. In the proposed formulation, the Gaussian random field is directly defined and sampled on the boundary of interest. An alternative strategy would consist in (1) solving the SPDE in the domain $C \setminus \Omega$, and (2) extracting nodal values on Γ. This second approach would, however, result in a much higher computational cost (with larger system matrices and values at the nodes that do not belong to Γ being ultimately discarded). In addition, sampling quality would be affected by the folding effects as Γ is a subset of the boundary ∂D.

2.3. Updating procedure based on conditional sampling

The boundedness of the state space $\mathcal{S}_\zeta$ for the non-Gaussian random field $\{\zeta(\boldsymbol{x}_\Gamma), \boldsymbol{x}_\Gamma \in \Gamma\}$ prevents perturbations from becoming too large. However, locally conflicting geometries, which are geometries leading to self-intersections in the finite element mesh, may be generated when the domain Ω contains (triangulated) faces that are close to one another. In the applications presented in Section 3.3 for instance, up to 5% of the nodes resulted in ill-conditioned meshes when large perturbation ranges were prescribed. The detection of intersections in a finite element mesh is an intricate issue, the discussion of which is beyond the scope of this paper; the interested reader is referred to, e.g., [64,65], for further detail. Surface perturbations resulting in conflicting geometries are not admissible and therefore have to be redrawn. Simply redrawing all nodes to generate a replacement surface perturbation is computationally inefficient because there is still a large likelihood that the replacement surface perturbation will have a conflicting geometry. To circumvent this drawback, only the nodes that contribute to conflicting geometries are updated. This is done while maintaining the correlation structure as follows.

Consider a reordering of the centered Gaussian vector $\boldsymbol{\Xi}$ of nodal values such that $\boldsymbol{\Xi} = (\boldsymbol{\Xi}^1; \boldsymbol{\Xi}^2)$, where semicolon denotes column-wise concatenation, $\boldsymbol{\Xi}^1$ is the Gaussian vector corresponding to perturbations resulting in conflicting geometries, and $\boldsymbol{\Xi}^2$ is the Gaussian vector associated with admissible perturbations. In practice, $\boldsymbol{\Xi}^1$ can be identified as the random vector of perturbations at the nodes where self-intersections are detected, or as the vector of perturbations that are associated with all nodes located within a few correlation ranges of the former set of nodes. Notice that the lengths of vectors $\boldsymbol{\Xi}^1$ and $\boldsymbol{\Xi}^2$ depend on both the size of the conflicting geometries and the (updated) realization under consideration. The goal is then to draw a new admissible sample of $\boldsymbol{\Xi}^1$ given the sample $\boldsymbol{\xi}^2$ of $\boldsymbol{\Xi}^2$. To this end, consider the associated partition of the covariance matrix $[\Sigma] = [Q]^{-1}$ of $\boldsymbol{\Xi}$:

$$[\Sigma] = \begin{bmatrix} [\Sigma^{11}] & [\Sigma^{12}] \\ [\Sigma^{21}] & [\Sigma^{22}] \end{bmatrix} . \tag{22}$$

Owing to the Gaussianity of $\boldsymbol{\Xi}$, it follows that

$$(\boldsymbol{\Xi}^1 | \boldsymbol{\Xi}^2 = \boldsymbol{\xi}^2) \sim \mathcal{N}(\overline{\boldsymbol{\mu}}, [\overline{\Sigma}]) \ , \tag{23}$$

in which

$$\overline{\boldsymbol{\mu}} = [\Sigma^{12}][\Sigma^{22}]^{-1}\boldsymbol{\xi}^2 \tag{24}$$

and

$$[\overline{\Sigma}] = [\Sigma^{11}] - [\Sigma^{12}][\Sigma^{22}]^{-1}[\Sigma^{21}] \ . \tag{25}$$

The sampling according to the conditional probability measure (see Eq. (23)) can efficiently be performed by using a factorization technique, since the random vector $\boldsymbol{\Xi}^1|\boldsymbol{\Xi}^2$ is often low-dimensional. In practice, the above procedure is applied in an iterative manner until an admissible sample of $\boldsymbol{\Xi}$ is obtained. In this approach, the computational cost mostly stems from the computation of the inverse matrix $[\Sigma^{22}]^{-1}$, which has to be estimated for each sample of $\boldsymbol{\Xi}$.

2.4. Construction of the transport map T

We now turn to the definition of the transport map T introduced in Section 2.1 that pushes forward the normally distributed random variable $\Xi(\boldsymbol{x}_\Gamma)$ to the non-Gaussian random variable $\zeta(\boldsymbol{x}_\Gamma)$ (see Eq. (2)), for $\boldsymbol{x}_\Gamma$ fixed on Γ. In order to simplify notation, space indexation is omitted in the rest of this section. The support of the probability density function p_ζ of ζ is written as $\mathcal{S}_\zeta = [\underline{\zeta}, \overline{\zeta}]$, where $\underline{\zeta}$ and $\overline{\zeta}$ are two given real numbers (with $\underline{\zeta} < \overline{\zeta}$). The probability density function p_ζ is determined below by using information theory [66] and the principle of maximum entropy [67], with the aim of obtaining an objective (that is, least informative) prior model.

The random variable ζ takes its values in $\mathcal{S}_\zeta$ and is assumed to satisfy the constraints

$$\mathbb{E}\{\log(\zeta - \underline{\zeta})\} = \underline{\nu} \ , \quad |\underline{\nu}| < +\infty \ , \tag{26}$$

and

$$\mathbb{E}\{\log(\overline{\zeta} - \zeta)\} = \overline{\nu} \ , \quad |\overline{\nu}| < +\infty \ . \tag{27}$$

It should be noticed that the values of $\underline{\nu}$ and $\overline{\nu}$ are irrelevant at this point to derive the explicit form of p_ζ. Following the principle of maximum entropy, the probability density function for ζ is then obtained as

$$p_\zeta(z) = I_{\mathcal{S}_\zeta}(z) c_0 (z - \underline{\zeta})^{-\underline{\lambda}} (\overline{\zeta} - z)^{-\overline{\lambda}} \ , \tag{28}$$

where $I_{\mathcal{S}_\zeta}$ is the indicator function of $\mathcal{S}_\zeta$, c_0 is the normalization constant, and $\underline{\lambda}$ and $\overline{\lambda}$ are the Lagrange multipliers associated with the constraints above. Let Y be the random variable defined as

$$Y = \frac{1}{\overline{\zeta} - \underline{\zeta}} (\zeta - \underline{\zeta}) \ . \tag{29}$$

It follows from Eqs. (28)–(29) that the probability density function of Y reads as

$$p_Y(y) = I_{[0,1]}(y) c_1 y^{-\underline{\lambda}} (1 - y)^{-\overline{\lambda}} \ , \tag{30}$$

where c_1 denotes the normalization constant. Eq. (30) shows that Y is a Beta random variable with parameters $\alpha = 1 - \underline{\lambda}$ and $\beta = 1 - \overline{\lambda}$, $Y \sim \mathcal{B}(\alpha, \beta)$. It can be deduced that

$$c_1 = \frac{1}{\mathbb{B}(1 - \underline{\lambda}, 1 - \overline{\lambda})} \ , \tag{31}$$

where $\mathbb{B}$ is the Beta function, and thus

$$c_0 = \frac{(\overline{\zeta} - \underline{\zeta})^{\underline{\lambda} + \overline{\lambda} - 1}}{\mathbb{B}(1 - \underline{\lambda}, 1 - \overline{\lambda})} \ . \tag{32}$$

The non-Gaussian random field $\{\zeta(\boldsymbol{x}_\Gamma), \boldsymbol{x}_\Gamma \in \Gamma\}$ can hence be defined as

$$\zeta(\boldsymbol{x}_\Gamma) = (\overline{\zeta} - \underline{\zeta}) F^{-1}_{\mathcal{B}(1-\underline{\lambda}, 1-\overline{\lambda})} \left(F_{\mathcal{N}(0,1)}(\Xi(\boldsymbol{x}_\Gamma)) \right) + \underline{\zeta} \ , \quad \forall \boldsymbol{x}_\Gamma \in \Gamma \ , \tag{33}$$

where $F^{-1}_{\mathcal{B}(1-\underline{\lambda}, 1-\overline{\lambda})}$ is the inverse cumulative distribution function of the Beta law with parameters $(1-\underline{\lambda})$ and $(1-\overline{\lambda})$, and $F_{\mathcal{N}(0,1)}$ is the cumulative distribution function of the normalized Gaussian distribution. Eq. (33) explicitly defines the mapping T.

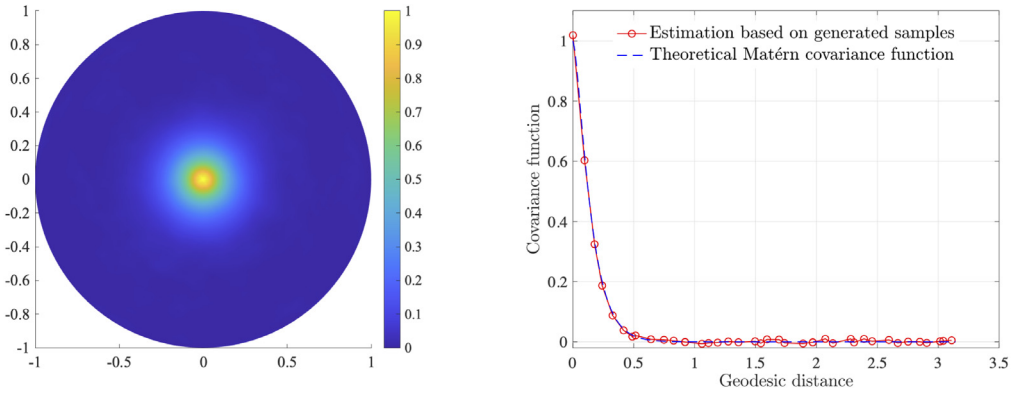

Fig. 2. Estimated covariance structure of the underlying Gaussian random field $\{\Xi(\boldsymbol{x}_\Gamma), \boldsymbol{x}_\Gamma \in \Gamma\}$ on the sphere. The estimated covariance function obtained by considering the north pole as the reference point is shown in the left panel (top view). The right panel displays a comparison between the estimated covariance function and the Matérn covariance function along a meridian of the sphere.

When similar constraints and symmetric perturbations are considered, one can take $\underline{\lambda} = \overline{\lambda} = \lambda$ (with $\lambda \leqslant 0$ since $\alpha, \beta \geqslant 1$) and $\underline{\zeta} = -\overline{\zeta} = -\varepsilon$ (perturbations are hence generated over $[-\varepsilon, \varepsilon]$), the above equation simplifies to

$$\zeta(\boldsymbol{x}_\Gamma) = 2\varepsilon F^{-1}_{\mathcal{B}(1-\lambda,1-\lambda)}\left(F_{\mathcal{N}(0,1)}(\Xi(\boldsymbol{x}_\Gamma))\right) - \varepsilon \ , \quad \forall \boldsymbol{x}_\Gamma \in \Gamma \ . \tag{34}$$

It follows that the random field is then centered

$$\mathbb{E}\{\zeta(\boldsymbol{x}_\Gamma)\} = 0 \ , \quad \forall \boldsymbol{x}_\Gamma \in \Gamma \ , \tag{35}$$

and has a pointwise variance

$$\mathrm{Var}\{\zeta(\boldsymbol{x}_\Gamma)\} = \frac{\varepsilon^2}{1+2\alpha} = \frac{\varepsilon^2}{3-2\lambda} \ , \quad \forall \boldsymbol{x}_\Gamma \in \Gamma \ . \tag{36}$$

In practice, Eq. (36) allows one to select the value of the Lagrange multiplier λ such that the field defining the geometrical perturbations exhibits a target variance. Notice that the pointwise variance decreases monotonically as α increases (or equivalently, as $\lambda \leqslant 0$ decreases), and its maximum value is $\varepsilon^2/3$ (which is obtained for $\lambda = 0$).

3. Applications

In all applications presented in this section, the parameter α is set to 2 and the Galerkin approach is deployed to solve the SPDE. All finite element meshes are constructed using GMSH [68]. Whenever studied, forward propagation of uncertainties is performed using a Monte Carlo approach. Discussions about other stochastic solvers are outside the scope of the present paper, and interested readers are referred to [69] for a review.

3.1. Application 1: Generation on a spherical shell

In order to exemplify the approach and validate the stochastic computational workflow, a random field of geometrical perturbations is first defined on the boundary Γ of a spherical domain Ω with radius $R = 0.45$ (which is a simple manifold in $\mathbb{R}^3$). It is assumed that $\eta = 0$ almost surely (recall that η represents homogeneous perturbations, so only spatially-dependent random perturbations are considered hereinafter), and that the perturbations at each point $\boldsymbol{x}_\Gamma$ are along the outward pointing normal direction $\boldsymbol{n}_\Gamma(\boldsymbol{x}_\Gamma)$ (that is, we take $\boldsymbol{d}_\Gamma(\boldsymbol{x}_\Gamma) := \boldsymbol{n}_\Gamma(\boldsymbol{x}_\Gamma)$ for all $\boldsymbol{x}_\Gamma$ in Γ). The boundary Γ is meshed with 60,350 linear triangular elements (30,182 nodes). The isotropic SPDE with $\ell = 0.1$ is solved to generate 50,000 samples of the underlying Gaussian random field $\{\Xi(\boldsymbol{x}_\Gamma), \boldsymbol{x}_\Gamma \in \Gamma\}$. The estimated covariance function with respect to a given point on the sphere is shown in Fig. 2. As expected, the correlation function is seen to be isotropic. Furthermore, the evolution of the correlation coefficient as a function of geodesic distance is consistent with the Matérn covariance function (see Eq. (3)) defined by a smoothness parameter ν set to 1 (recall that $\alpha = \nu + d/2$, with $\alpha = 2$ and $d = 2$ here).

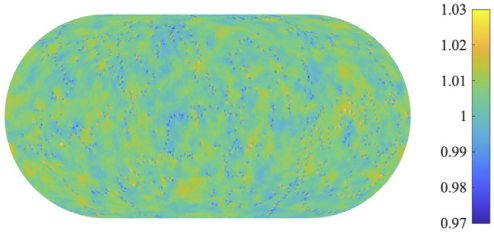

Fig. 3. Graph of the pointwise standard deviation for the underlying Gaussian random field $\{\Xi(\boldsymbol{x}_\Gamma), \boldsymbol{x}_\Gamma \in \Gamma\}$ on the sphere. Minimum and maximum values for the standard deviation are 0.97 and 1.03, respectively.

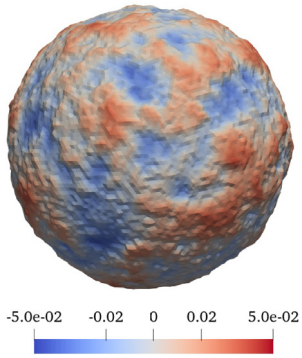

Fig. 4. One realization of the sphere with geometrical imperfections. Centered perturbations are considered, with $\underline{\zeta} = -0.05$ and $\overline{\zeta} = 0.05$. The standard deviation of the perturbation field is set to 0.15.

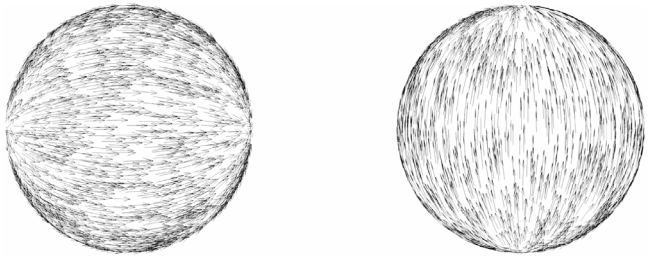

Fig. 5. Graph of the orientation fields $\boldsymbol{x}_\Gamma \mapsto \boldsymbol{e}^1(\boldsymbol{x}_\Gamma)$ (left) and $\boldsymbol{x}_\Gamma \mapsto \boldsymbol{e}^2(\boldsymbol{x}_\Gamma)$ (right).

The pointwise standard deviation estimated with the 50,000 samples is shown in Fig. 3, using an Eckert IV projection of the spherical shell. Since the spherical boundary Γ is a closed manifold, it is seen that the standard deviation remains fairly uniform and close to 1. The observed minor spatial fluctuations in the standard deviation field are primarily induced by finite sampling and can be reduced by increasing the number of samples.

The realizations of the Gaussian seed are subsequently mapped to first obtain the associated realizations of the non-Gaussian field $\{\zeta(\boldsymbol{x}_\Gamma), \boldsymbol{x}_\Gamma \in \Gamma\}$ (see Eq. (33)), and then to compute samples of the randomly perturbed manifold $\widetilde{\Gamma}$ according to Eq. (1). A realization of the perturbed spherical boundary, defined by the support $\mathcal{S}_\zeta = [-0.05, 0.05]$ for the perturbations and a standard deviation equal to 0.15, is shown in Fig. 4.

For the sake of completeness, we next consider the sampling of an anisotropic random field. To this end, the matrix-valued diffusion field is constructed by following the methodology described in 2.2.3. Specifically, the sphere is embedded in a cube, and two Laplace problems are solved in order to compute the orientation fields along the latitude and longitude. These two fields are denoted by $\boldsymbol{x}_\Gamma \mapsto \boldsymbol{e}^1(\boldsymbol{x}_\Gamma)$ and $\boldsymbol{x}_\Gamma \mapsto \boldsymbol{e}^2(\boldsymbol{x}_\Gamma)$, respectively, and are shown in Fig. 5. Different anisotropic fields can then be generated by adjusting the parameters λ_1 and λ_2 in the diffusion field (see Eq. (11)). Realizations and correlation functions obtained by selecting $\lambda_1 \gg \lambda_2$ or $\lambda_1 \ll \lambda_2$ are shown in Figs. 6 and 7, respectively. It is seen, in particular, that the former selection generates long-range spatial

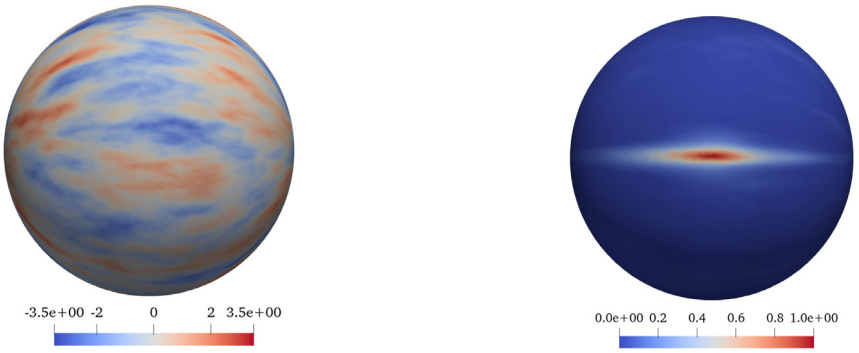

Fig. 6. Realization (left) and estimated correlation function (right) of the underlying Gaussian random field, obtained for $\lambda_1 = 1$ and $\lambda_2 = 0.1$. Setting $\lambda_1 \gg \lambda_2$ creates a specific signature along the latitude.

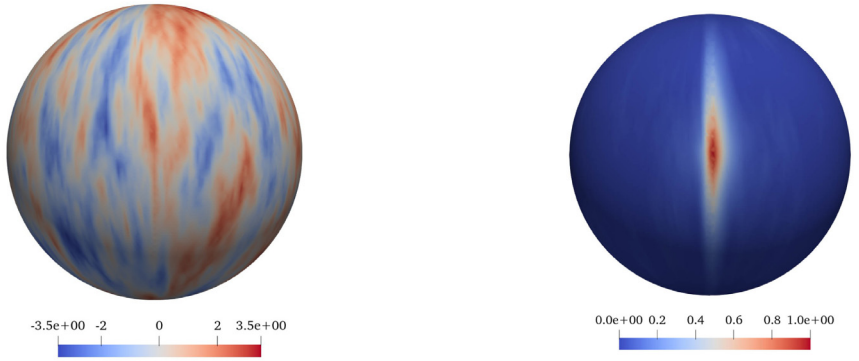

Fig. 7. Realization (left) and estimated correlation function (right) of the underlying Gaussian random field, obtained for $\lambda_1 = 0.1$ and $\lambda_2 = 1$. Setting $\lambda_1 \ll \lambda_2$ creates a specific signature along the longitude.

memory along the latitude, while the latter choice enables a similar effect along the longitude. In practice, the simple and low-dimensional, physically-interpretable parameterization of the diffusion field allows one to readily formulate forward propagation analysis (and statistical inverse problems) on more complex domains. This capability of the stochastic modeling framework is exemplified in Sections 3.2 and 3.3 respectively, where the cases of patient-specific brain geometries and structures processed by additive manufacturing are addressed.

Remark. For the spherical case under investigation, standard models based on, e.g., Karhunen–Loève expansions can be used to define and generate the field. Adopting a spherical coordinate system (R, θ, ϕ) (for a given radius R), one may adopt a separable covariance function for instance, defining C as

$$C((R,\theta_1,\phi_1),(R,\theta_2,\phi_2)) = C_\theta(\theta_1,\theta_2) \times C_\phi(\phi_1,\phi_2) \ , \tag{37}$$

where C_θ and C_ϕ are one-dimensional (e.g., exponential-type) covariance functions satisfying appropriate evenness and periodicity requirements; see, e.g., [70]. Likewise, the case of cylindrical interfaces can be handled by using a separable structure with one-dimensional covariance functions expressed in terms of the axial distance and azimuth; see the references focused on, e.g., cylindrical shells in Section 1.

3.2. Application 2: Modeling of geometrical imperfections induced by additive manufacturing

Additive manufacturing (AM), or 3D printing, is now commonly employed in a variety of fields in engineering, including aerospace, biomedical, construction, and mechanical industries at large. While AM technologies have enabled the production of parts with unprecedented levels of complexity over multiple scales, processing challenges remain numerous [29,71,72]. In particular, the generation of local (e.g., solidification) defects, anisotropic material

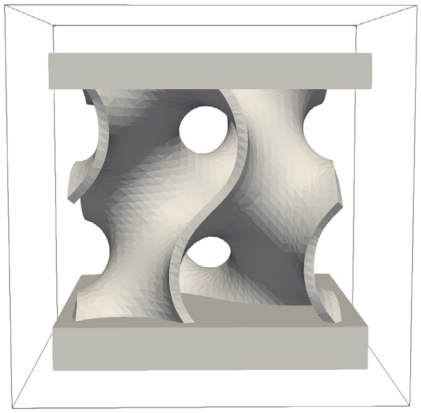

Fig. 8. Nominal gyroid model, immersed in the box used to solve the Laplace problems ((x, y) plane is horizontal).

behavior, and geometrical imperfections is often faced and can dramatically impact the mechanical performance of the AM structure. This aim of this section is then to demonstrate the use of the proposed framework to model and generate process-induced geometrical imperfections on a structure produced by additive manufacturing. To this end, we consider a titanium gyroid structure produced by selective laser melting as a prototypical case relevant to bone tissue engineering [73]. The size of the unit cell is $3.2 \times 3.2 \times 3.2$ [mm] and wall depth is set to 0.12 [mm]. In order to enable mechanical testing using finite element simulations, thick plates are added at the top and bottom of the structure, as shown in Fig. 8. The finite element size for the gyroid model is set to 0.05 [mm], in accordance with the mean height of the layers created by the AM process, and the mesh comprises 139,424 $\mathbb{P}_1$ triangular elements and 69,696 nodes.

In order to set up the underlying Gaussian random field model, and following specifications from the manufacturing process, we assume that the geometrical imperfections are generated layer-wise in the (x, y) plane and exhibit spatial correlation along the two-dimensional contour. To sample the field, we then use the anisotropic SPDE given by Eq. (11), defining the diffusion field in Eq. (12) with $d = 2$, $\lambda_1 = 1$ and $\lambda_2 = \epsilon$ (with $\epsilon \ll 1$). Here, the small parameter ϵ is introduced to ensure the positive-definiteness of the diffusion matrix whenever the orientation vectors are (nearly) orthogonal. The orientation vector field $\boldsymbol{e}^1$ is specifically defined as

$$\boldsymbol{e}^1(\boldsymbol{x}_\Gamma) = \boldsymbol{t}(\boldsymbol{x}_\Gamma) \ , \quad \forall \boldsymbol{x}_\Gamma \in \Gamma \ , \tag{38}$$

where $\boldsymbol{t}(\boldsymbol{x}_\Gamma)$ is the unit vector tangent to the two-dimensional contour at location $\boldsymbol{x}_\Gamma$ in the (x, y) plane. The field of tangent vectors is obtained by first solving the Laplace problem (see Section 2.2.3) with Dirichlet boundary conditions enforced either at the left ($\Psi = 0$) and right ($\Psi = 1$) faces, or at the back and front faces, and by subsequently projecting (and normalizing) the vector field thus obtained onto the (x, y) plane. The second orientation vector field $\boldsymbol{e}^2$ is obtained by solving the Laplace problem with essential boundary conditions applied at the bottom ($\Psi = 0$) and top ($\Psi = 1$) faces. One realization of the Gaussian seed $\{\Xi(\boldsymbol{x}_\Gamma), \boldsymbol{x}_\Gamma \in \Gamma\}$ and the correlation function estimated on the boundary Γ (with a reference point arbitrarily chosen on Γ) for a small value of the correlation parameter ℓ are shown in Fig. 9. As expected, it is seen that the correlation is non-vanishing along the in-plane contour, hence generating realizations that are consistent with the underlying physical process. It should be noticed that the determination of model parameters, such as the correlation parameter ℓ, for a particular additive manufacturing process is outside the scope of this work and is therefore left for future research.

Following the methodology presented in Section 2.1, realizations of the Gaussian random field on the gyroid surface are next pushed forward to obtain realizations of $\{\zeta(\boldsymbol{x}_\Gamma), \boldsymbol{x}_\Gamma \in \Gamma\}$, using the mapping defined in Eq. (34) with $\varepsilon = 0.03$ [mm] (meaning that the support for the oscillatory perturbations is $\mathcal{S}_\zeta = [-0.03, 0.03]$). In addition, a homogeneous perturbation is considered to account for the variations in porosity that can typically be observed with highly-porous structures produced by AM [73]. For the sake of illustration, we assume that η is uniformly distributed on $\mathcal{S}_\eta = [-0.02, 0.02]$ [mm], $\eta \sim \mathcal{U}(-0.02, 0.02)$ [mm]. Finally, the direction of the perturbations given by the field $\boldsymbol{x}_\Gamma \mapsto \boldsymbol{d}_\Gamma(\boldsymbol{x}_\Gamma)$ can be inferred from the specifications of the manufacturing process. In the case of titanium scaffolds produced by selective laser melting, scanning paths, while parallel within a single depository

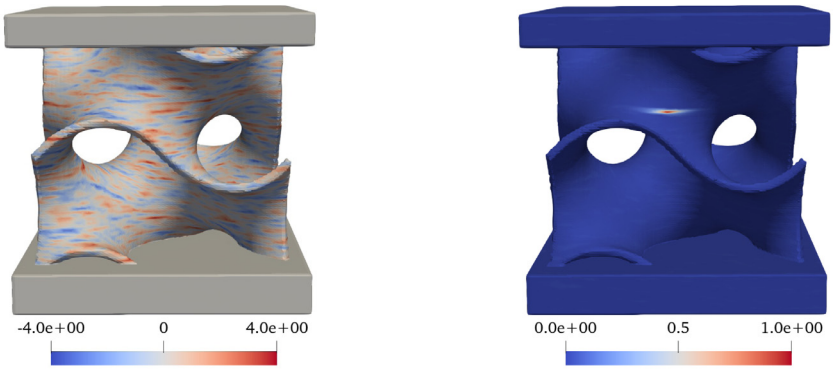

Fig. 9. Realization of the underlying Gaussian random field (left panel) and correlation function on the gyroid surface (right panel), obtained for $\lambda_1 = 1$, $\lambda_2 = 1e{-}6$, and $\ell = 0.1$ [mm].

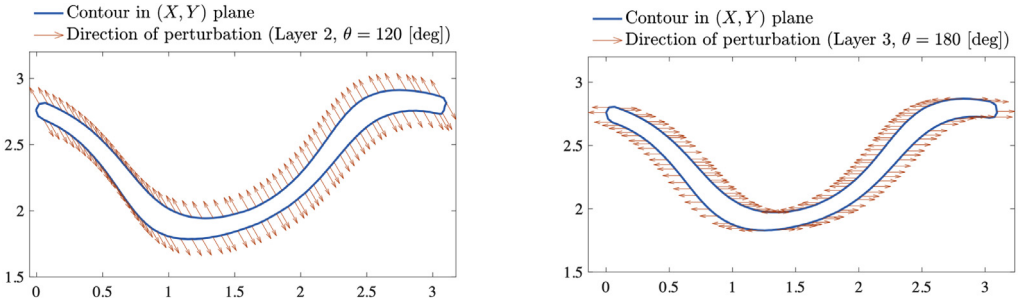

Fig. 10. Perturbation directions on two successive layers. The direction of the geometrical perturbations is rotated by an angle of 60 degrees from one layer to the next, according to the specification of the AM manufacturing process.

layer, are rotated by a fixed angle between layers. This procedure, which is similar to unidirectional plies stacking in layered composites, leads to a fairly isotropic material behavior at the macroscopic scale. We hence define the direction of the perturbation within the layer k, denoted by $\boldsymbol{d}^k_\Gamma(\boldsymbol{x}_\Gamma)$, as

$$\boldsymbol{d}^k_\Gamma(\boldsymbol{x}_\Gamma) = (\cos(\theta_k), \sin(\theta_k), 0)^\mathsf{T} \ , \tag{39}$$

where $\theta_{k+1} = \theta_k + 60$ for $k \geqslant 1$ and $\theta_1 = 0$ [deg]. Examples of the vector field $\boldsymbol{x}_\Gamma \mapsto \boldsymbol{d}_\Gamma(\boldsymbol{x}_\Gamma)$ are shown along the two-dimensional contour for two successive layers in Fig. 10. The height of each layer is set to 0.05 [mm], which is a typical value in AM processes. Each node in the finite element mesh is then assigned a specific layer, and thus a perturbation direction according to Eq. (39), based on its vertical coordinate. In the unlikely case where one node is exactly located at the boundary between subsequent layers, the direction associated with the lower layer is chosen by default.

It should be noticed that the spatially-dependent geometrical uncertainties thus generated remain small as compared to the structural characteristic lengths and are hardly visible on a three-dimensional plot. They, however, have a substantial impact on the mechanical behavior of the structure, due to its high porosity rate. We consider a tensile test with a zero displacement boundary condition at the bottom surface and a vertical displacement of magnitude 0.03 [mm] at the top surface. The stochastic boundary value problem therefore reads as

$$\left\{ \begin{array}{l} \mathrm{div}([\boldsymbol{\Sigma}]) = \boldsymbol{0} \ , \quad \forall \boldsymbol{x} \in \Omega \ , \\ [\boldsymbol{\Sigma}(\boldsymbol{x})] = [\![\boldsymbol{C}]\!] : [\boldsymbol{\mathcal{E}}(\boldsymbol{x})] \ , \quad \forall \boldsymbol{x} \in \Omega \ , \\ [\boldsymbol{\mathcal{E}}(\boldsymbol{x})] = \boldsymbol{\nabla}^{\mathrm{S}}_{\boldsymbol{x}} \boldsymbol{u}(\boldsymbol{x}) \ , \quad \forall \boldsymbol{x} \in \Omega \ , \end{array} \right. \tag{40}$$

subjected to $\boldsymbol{u} = \boldsymbol{0}$ at the bottom surface and $\boldsymbol{u} = (0, 0, 0.03)^\mathsf{T}$ [mm] at the top surface. In Eq. (40), $[\boldsymbol{\Sigma}]$ and $[\boldsymbol{\mathcal{E}}]$ are the Cauchy stress and linearized strain tensors, respectively, the symbol $\boldsymbol{\nabla}^{\mathrm{S}}_{\boldsymbol{x}}$ denotes symmetrized gradient, $\boldsymbol{u} = (u_1, u_2, u_3)^\mathsf{T}$ is the displacement vector, $[\![\boldsymbol{C}]\!]$ is the isotropic elasticity tensor, and Ω denotes the domain with

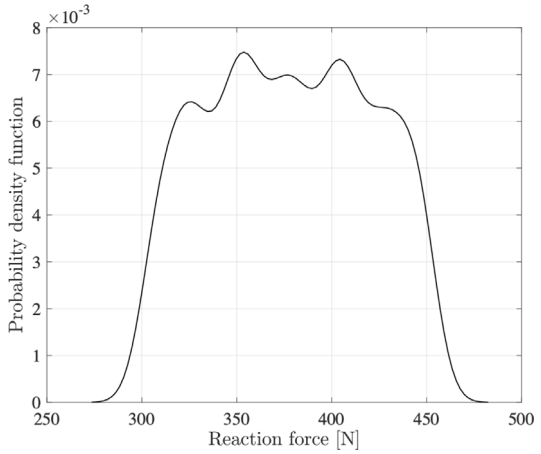

Fig. 11. Probability density distribution of the reaction force estimated with 8000 realizations of the perturbation random field.

perturbed boundary. Following standard characteristics for 3D printed titanium, the Young's modulus of the material is set to 110 [GPa], and the Poisson's ratio is taken as 0.3. The reaction force on the top face is evaluated by the finite element method, using a set of 8000 independent realizations sampled with the parameters detailed above. The mesh used for the mechanical simulations contains approximately 120,000 $\mathbb{P}_1$ tetrahedral elements and 32,000 nodes, depending on the realization of the gyroid model. The probability distribution function of the reaction force is shown in Fig. 11. It is seen that the variability in the mechanical response is significant, the reaction force exhibiting a coefficient of variation of 0.11. While such qualitative outcomes must be put into perspective and would require, in particular, additional developments focusing on parameter identification and validation of uncertainty propagation results (these developments are beyond the scope of the proposed study), the results demonstrate the capability of the stochastic framework to efficiently perform uncertainty quantification integrating process-related information on complex domains produced by additive manufacturing.

3.3. Application 3: Modeling of segmentation errors in magnetic resonance imaging

Numerical simulations for non-invasive brain stimulation methods, such as the transcranial magnetic stimulation (TMS) [74,75] and transcranial electrical stimulation (TES) [76] methods, are becoming widespread tools for protocol design and diagnosis. In these studies, images obtained from magnetic resonance imaging (MRI) are typically used in conjunction to fMRI pipelines (such as freeSurfer [77] or SPM [78]) to generate head models. The accuracy of such simulations strongly depends on the fidelity of the brain model, which is usually obtained from a segmentation process on MRI brain images (see [79–81] for automated segmentation packages for brain anatomy). While the existence of segmentation uncertainties in brain tissue boundaries has been reported in several studies [82–84], little work has been devoted to the proper modeling and propagation of spatially-dependent geometrical uncertainties in TMS-related simulations, due in part to the complexity of the geometries involved (see [74] for an analysis on the cortical surface, using random but homogeneous uncertainties). We therefore turn our attention to the modeling of segmentation errors in MRI in this section. The aim is to demonstrate the ability of the proposed framework to properly define and generate tissue surface uncertainties. We specifically consider the boundary between the skull and the cerebrospinal fluid (CSF), as well as the boundary between the CSF and gray matter (GM)—as both were shown to have substantial impact on the electric fields (E-fields) generated during TMS. Note that sampling is performed on the anatomy provided by the MRI, and may include additional (e.g., spinal cord) interfaces. The latter will not be considered in TMS simulations (see Section 3.3.4). Throughout this section, we only consider oscillatory perturbations and accordingly set $\eta = 0$ almost surely.

3.3.1. Generation of the underlying Gaussian random field on the Bone/CSF interface

We first consider the definition and generation of the underlying Gaussian random field $\{\Xi(\boldsymbol{x}_\Gamma), \boldsymbol{x}_\Gamma \in \Gamma\}$ at the interface between the bone and the cerebrospinal fluid (denoted by Bone/CSF interface). The discretization of

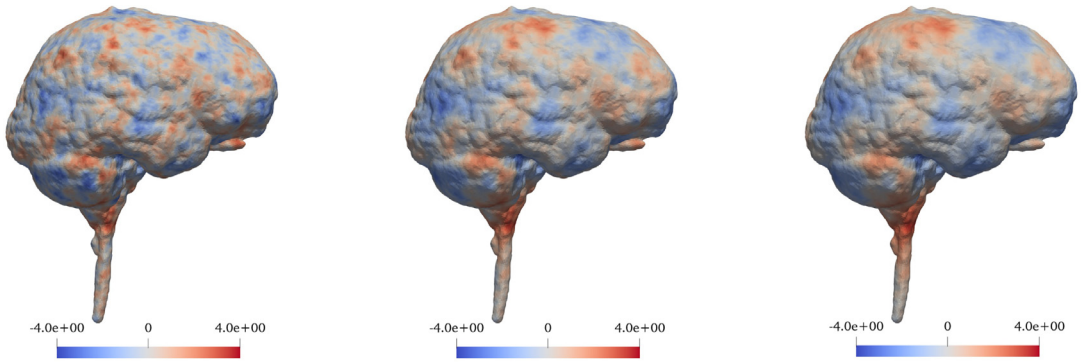

Fig. 12. Realizations of the Gaussian random field $\{\Xi(\boldsymbol{x}_\Gamma), \boldsymbol{x}_\Gamma \in \Gamma\}$ at the Bone/CSF interface, obtained with $\ell = 5$ [mm] (left), $\ell = 10$ [mm] (middle), and $\ell = 15$ [mm] (right). These realizations are generated by using a Cholesky factorization technique with the precision matrix $[Q]$ and the *same* realization of a normalized Gaussian random vector, for the sake of comparison.

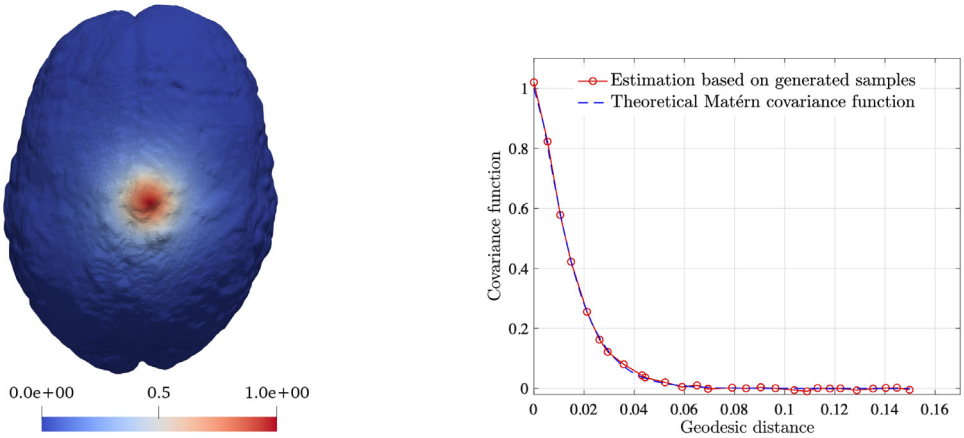

Fig. 13. Estimated covariance structure of the underlying Gaussian random field $\{\Xi(\boldsymbol{x}_\Gamma), \boldsymbol{x}_\Gamma \in \Gamma\}$ at the Bone/CSF interface. The left panel displays the covariance function estimated on the manifold (the reference point is selected arbitrarily on the top of the surface). The comparison between the estimated covariance function and the Matérn covariance function along a certain path on the manifold is shown in the right panel.

the interface is performed by using a $\mathbb{P}_1$ triangular mesh with 41,561 nodes and 83,118 elements. Realizations of the underlying Gaussian random field computed with the correlation length parameter ℓ set to $5, 10, 15$ [mm] respectively are shown in Fig. 12. Notice that the same seed is used to initialize the random generation for all configurations, so that samples can be compared qualitatively. It is seen that the framework is able to generate realizations that capture the geometrical features of the boundary, and that larger values of correlation parameter ℓ result in smoother variations on the manifold.

The covariance function estimated with 50,000 independent samples is next shown in Fig. 13 for $\ell = 10$ [mm] (in this figure, the reference point is randomly chosen on the interface). It is observed that the computed covariance function is isotropic on the manifold and matches the theoretical Matérn covariance function, defined with respect to the geodesic distance. In this application, the geodesic distance was calculated by using the heat method [85].

3.3.2. Generation of the underlying Gaussian random field on the CSF/GM interface

Here, the definition and sampling of the underlying Gaussian random field on the CSF and GM cortical interface (denoted as the CSF/GM interface) is studied. The cortical surface consists of many folds with complicated bends. In order to accurately discretize these folds, high-resolution meshes are required. In the present case, a standard cortical boundary mesh that consists of 137,518 nodes and 275,032 $\mathbb{P}_1$ finite elements is used. Note that this is much

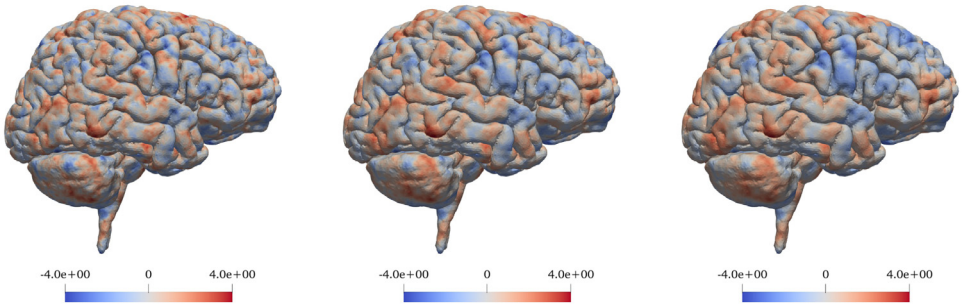

Fig. 14. Realizations of the Gaussian random field $\{\Xi(\boldsymbol{x}_\Gamma), \boldsymbol{x}_\Gamma \in \Gamma\}$ at the CSF/GM interface, obtained with $\ell = 3$ [mm] (left), $\ell = 5$ [mm] (middle), and $\ell = 7$ [mm] (right). These realizations are generated by using a Cholesky factorization technique with the precision matrix $[Q]$ and the *same* realization of a normalized Gaussian random vector, for the sake of comparison.

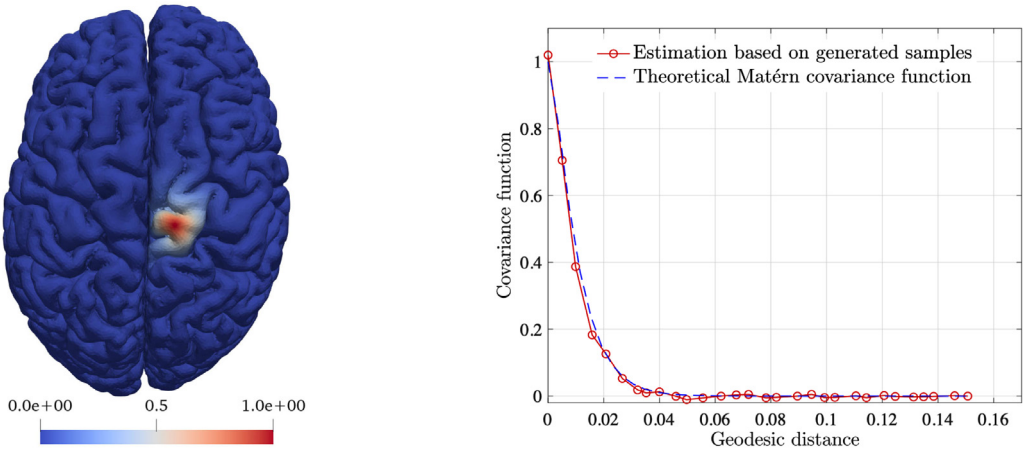

Fig. 15. Estimated covariance structure of the underlying Gaussian random field $\{\Xi(\boldsymbol{x}_\Gamma), \boldsymbol{x}_\Gamma \in \Gamma\}$ at the CSF/GM interface, for $\ell = 7$ [mm]. The left panel displays the covariance function estimated on the manifold: here, a node close to the separation plane between the hemispheres is selected as the reference point. The comparison between the estimated covariance function and the Matérn covariance function along a certain path on the manifold is shown in the right panel.

larger than the 41,562-node mesh used for the Bone/CSF interface. Furthermore, adjacent folds are oftentimes close to each other resulting in a large probability of inadmissible, self-intersecting realizations. As a result, the updating scheme developed in this manuscript becomes essential for the practical generation of cortex boundary uncertainty.

Fig. 14 shows realizations of the Gaussian random field $\{\Xi(\boldsymbol{x}_\Gamma), \boldsymbol{x}_\Gamma \in \Gamma\}$ generated at the cortex for various values of the correlation hyperparameter ℓ. As expected, realizations for higher values of ℓ appear smoother as they exhibit larger correlation ranges. This figure illustrates the capability of the framework to capture very complex geometrical features.

The covariance function, defined by randomly choosing a reference point on the cortex, was computed from 50,000 independent realizations of the Gaussian random field, and is shown in Fig. 15 (left panel). Unlike previous examples, the region of non-vanishing correlation coefficients is not circular, even if the isotropic SPDE is used for sampling purposes. This distribution is indeed due to the varying depths of the cortical folds. The estimated covariance function also matches its theoretical Matérn counterpart parameterized with the geodesic distance, as seen in the right panel in Fig. 15.

In terms of computational time, about 65 s are necessary to draw 1000 samples on a desktop computer equipped with an AMD Ryzen 3600 6-core processor (cadenced at 3.59 GHz) and 16 GB of memory. About 25% of this computational time is allocated to the computation of the precision matrix $[Q]$ and its Cholesky decomposition, the rest of the time being spent for solving the linear system $[R]\boldsymbol{u} = \boldsymbol{w}$; see the last paragraph at the end of Section 2.2.1.

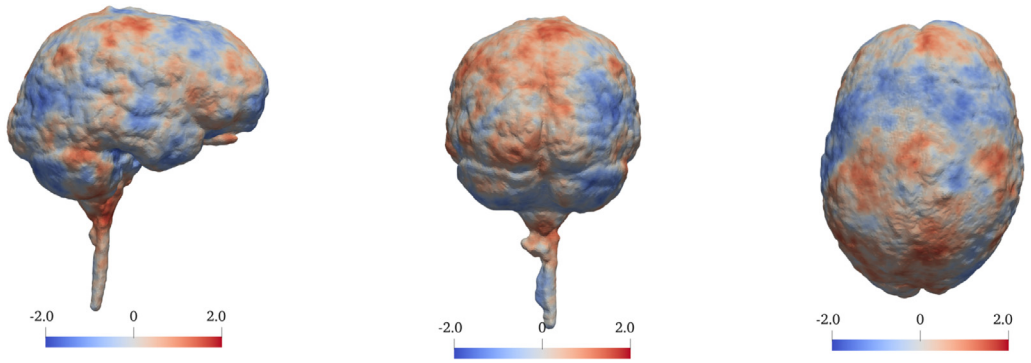

Fig. 16. Plot of one realization of the perturbed geometry (height in millimeters) $\{\boldsymbol{X}_{\tilde{\Gamma}}(\boldsymbol{x}_\Gamma), \boldsymbol{x}_\Gamma \in \Gamma\}$ at the Bone/CSF interface.

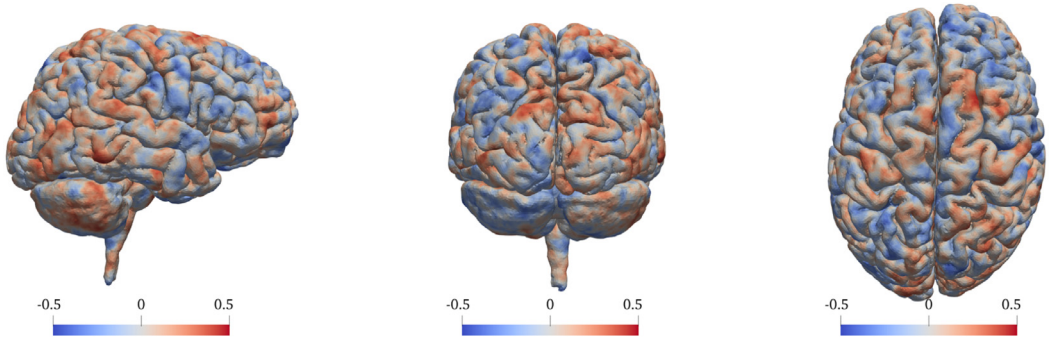

Fig. 17. Plot of one realization of the perturbed geometry (height in millimeters) $\{\boldsymbol{X}_{\tilde{\Gamma}}(\boldsymbol{x}_\Gamma), \boldsymbol{x}_\Gamma \in \Gamma\}$ at the CSF/GM interface.

3.3.3. Generation of perturbed Bone/CSF and CSF/GM interfaces

Here we provide examples of realizations obtained for the perturbed manifolds at the Bone/CSF and CSF/GM interfaces. The typical resolution of MRI is 1 [mm], and there is experimental evidence indicating that processing algorithms have an uncertainty of 0.2 [mm] for cortical surfaces [82–84]. Hence, in the following simulations, we set the range of perturbations as $\mathcal{S}_\zeta = [-2, 2]$ [mm] and $\mathcal{S}_\zeta = [-0.5, 0.5]$ [mm] for the Bone/CSF and CSF/GM interfaces, respectively. The correlation parameter is set to $\ell = 10$ [mm] for the Bone/CSF boundary, while $\ell = 5$ [mm] for the CSF/GM interface. Note that parametric studies to quantify the sensitivity of computational models to such properties on quantities of interest are beyond the scope of this work and are left for future works. The nominal surfaces are perturbed along the normal direction, that is, we take $\boldsymbol{d}_\Gamma(\boldsymbol{x}_\Gamma) := \boldsymbol{n}_\Gamma(\boldsymbol{x}_\Gamma)$ for all $\boldsymbol{x}_\Gamma$ in Γ, with $\boldsymbol{n}_\Gamma(\boldsymbol{x}_\Gamma)$ the outward-pointing unit normal to the surface Γ at location $\boldsymbol{x}_\Gamma$. Realizations of the perturbed Bone/CSF and CSF/GM interfaces are shown in Figs. 16 and 17, respectively.

3.3.4. Propagation of geometrical uncertainties on brain interfaces

In this section, we finally perform uncertainty propagation for TMS simulation results by using a Monte Carlo approach. TMS simulations aim to simulate the electrical field (E-field) inside the brain tissues induced by a driven magnetic coil above the head. The typical implementation configuration of TMS is shown in Fig. 18, where the coil is placed over the motor cortex region (the yellow box region).

During TMS, a coil is driven with known currents

$$\boldsymbol{J}(\boldsymbol{r}; t) = p(t)\boldsymbol{J}(\boldsymbol{r}) \,, \tag{41}$$

where $t \mapsto p(t)$ the current pulse temporal variation and $\boldsymbol{r} \mapsto \boldsymbol{J}(\boldsymbol{r})$ is a time independent current density, induces an E-field

$$\boldsymbol{E}_{\text{tot}}(\boldsymbol{r}; t) = \frac{dp(t)}{dt}\boldsymbol{E}_{\text{tot}}(\boldsymbol{r}) \tag{42}$$

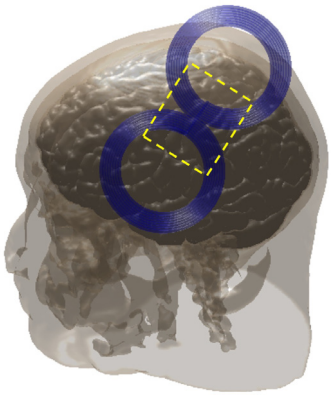

Fig. 18. The TMS experiment configuration: the coil is placed on the scalp above the motor cortex, and the yellow dashed box indicates the gray matter region where the E-field is shown in the subsequent figures.

inside the head (notice the slight abuse of notation). The E-field $\boldsymbol{r} \mapsto \boldsymbol{E}_{\text{tot}}(\boldsymbol{r})$ is then decomposed into the sum of two components, called the primary and secondary E-fields. The primary E-field $\boldsymbol{r} \mapsto \boldsymbol{E}_p(\boldsymbol{r})$ is the E-field induced by the coil currents in a vacuum and can be found from the Biot–Savart law as

$$\boldsymbol{E}_p(\boldsymbol{r}) = \frac{\mu_0}{4\pi} \int \frac{\boldsymbol{J}(\boldsymbol{r}')}{\|\boldsymbol{r} - \boldsymbol{r}'\|} d\boldsymbol{r}' \ , \tag{43}$$

where μ_0 is the permeability of free-space. The secondary E-field $\boldsymbol{r} \mapsto \boldsymbol{E}_s(\boldsymbol{r})$ results from charges building up in tissue interfaces and can be determined as

$$\boldsymbol{E}_s(\boldsymbol{r}) = -\nabla \frac{1}{4\pi\epsilon_0} \int \frac{\rho(\boldsymbol{r}')}{\|\boldsymbol{r} - \boldsymbol{r}'\|} d\boldsymbol{r}' \ , \tag{44}$$

where ϵ_0 is the permittivity of free-space and $\boldsymbol{r} \mapsto \rho(\boldsymbol{r})$ is an unknown charge density residing on tissue boundaries. At each interface, the charge density is determined by applying the electromagnetic boundary condition

$$\langle \boldsymbol{n}, \sigma^+ \boldsymbol{E}^+_{\text{tot}} \rangle = \langle \boldsymbol{n}, \sigma^- \boldsymbol{E}^-_{\text{tot}} \rangle \ , \tag{45}$$

where $\boldsymbol{n}$ is the outward unit vector normal to the boundary, $\langle \boldsymbol{n}, \boldsymbol{E}^+_{\text{tot}} \rangle$ and $\langle \boldsymbol{n}, \boldsymbol{E}^-_{\text{tot}} \rangle$ are the total electric field along the normal direction an infinitesimal away from the tissue boundary into the outer and inner head tissue compartment, respectively, and σ^- and σ^+ are the conductivities of the inner and outer head tissue compartments, respectively. The above boundary condition results in the following integral equation defined on each tissue boundary

$$\frac{1}{2}\rho(\boldsymbol{r}) + \mathcal{J}(\sigma)\langle \frac{1}{4\pi} \int_{p.v.} \rho(\boldsymbol{r}') \frac{\boldsymbol{r} - \boldsymbol{r}'}{\|\boldsymbol{r} - \boldsymbol{r}'\|^3} d\boldsymbol{r}', \boldsymbol{n}(\boldsymbol{r}) \rangle = -\mathcal{J}(\sigma)\epsilon_0 \langle \boldsymbol{E}_p(\boldsymbol{r}), \boldsymbol{n}(\boldsymbol{r}) \rangle \ , \tag{46}$$

where $\mathcal{J}(\sigma) = (\sigma^+ - \sigma^-)/(\sigma^+ + \sigma^-)$ and "$p.v.$" is used to denote Cauchy principal value. In this work, the boundary element method (BEM) described in [86] is used to solve Eq. (46) for the charge distribution $\boldsymbol{r} \mapsto \rho(\boldsymbol{r})$ on the interface. In Eq. (46), the charge distribution is defined on tissue interfaces and as a result, the TMS simulation can be conducted only using the boundary mesh of brain tissue interfaces, without generating volume mesh in the brain, which reduces the computation cost greatly. The BEM solver used here is freely-available online (see [87]), and implementation details can be found in [86].

As mentioned above, the bounds for the geometrical uncertainty are set to $\underline{\zeta} = -\overline{\zeta} = -0.5$ [mm] and $\underline{\zeta} = -\overline{\zeta} = -0.1$ [mm], and the correlation lengths to $\ell = 10$ [mm] and $\ell = 5$ [mm], for the Bone/CSF and CSF/GM interfaces, respectively. Some statistical estimators based on the Monte-Carlo approach results (with 1000 simulations) are shown in Fig. 19. The E-field has a peak variance of 19.1 [V/m], indicating a significant impact of the uncertainties in the E-field distribution. This suggests that stochastic simulations accounting for geometrical uncertainties can provide useful information to better assess E-field properties and thereby optimize clinical procedures on patient-specific brain geometries. Notice that parametric studies characterizing the influence of MRI data segmentation uncertainties on TMS simulation more broadly are beyond the scope of this work and will be addressed in future work.

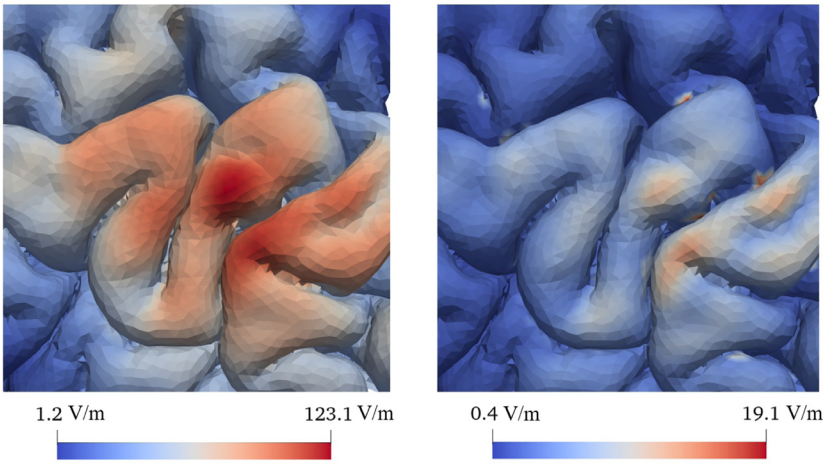

Fig. 19. E-field distribution on the CSF/GM brain interface obtained from the Monte Carlo simulations. The left panel shows the mean field, and the left panel shows the standard deviation distribution. Both of the geometries of the Bone/CSF and CSF/GM interfaces are modified according to the non-Gaussian field. The perturbation range is $[-0.5, 0.5]$ [mm] (with $\ell = 10$ [mm]) on the Bone/CSF interface, and is set to $[-0.1, 0.1]$ [mm] (with $\ell = 5$ [mm]) on the CSF/GM interface.

4. Conclusion

The ability to produce and analyze complex geometries with features spanning a wide range of scales has become widespread with the advent of new processing technologies such as additive manufacturing. This setting offers new challenges from a stochastic modeling standpoint, since appropriate covariance functions become hard to define in closed form a priori—hence making commonly employed frameworks to account for spatially-dependent geometrical uncertainties potentially unpractical.

Motivated by these observations, we presented a framework to efficiently represent and simulate spatially-dependent geometrical uncertainties on complex domains. Following previous works focused on stochastic constitutive modeling by the authors, the methodology builds upon the combination of a stochastic partial differential equation approach and an information-theoretic model to ensure well-posedness while capturing salient geometrical features on the fly. In particular, the proposed approach allows the random field to be defined and directly sampled on the manifold corresponding to the nominal interface—hence leading to substantial savings in terms of computational cost. In addition, we derived a procedure to efficiently update perturbations resulting in self-intersection in the finite element mesh. We finally discussed model parameterization and numerical results in the form of sampling verification and forward propagation problems on challenging applications, including the case of a porous part produced by additive manufacturing and patient-specific brain interfaces.

The framework paves the way towards the integration of topological perturbations on complex domains, and several avenues for further development include: (1) experimentally-based parameter identification and validation on selected applications; (2) geometrically-informed forward propagation and sensitivity analyses; (3) the sophistication of the proposed representation to account for, e.g., stochastic directions of perturbation; and (4) the construction of fast sampling algorithms for poorly conditioned systems.

Declaration of competing interest

The authors declare that they have no known competing financial interests or personal relationships that could have appeared to influence the work reported in this paper.

Acknowledgments

The work of the J.G. was partially supported by the National Science Foundation, USA, Division of Civil, Mechanical and Manufacturing Innovation, under award CMMI-1942928. The work of L.G. was supported by the National Institute of Mental Health, USA, award 4R00MH120046. The content of current research is solely

the responsibility of the authors and does not necessarily represent the official views of the National Institutes of Health. The authors would like to thank the reviewers for insightful comments that helped improving the readability of the paper.

References

[1] A. Vakis, V. Yastrebov, J. Scheibert, L. Nicola, D. Dini, C. Minfray, A. Almqvist, M. Paggi, S. Lee, G. Limbert, J. Molinari, G. Anciaux, R. Aghababaei, S. Echeverri Restrepo, A. Papangelo, A. Cammarata, P. Nicolini, C. Putignano, G. Carbone, S. Stupkiewicz, J. Lengiewicz, G. Costagliola, F. Bosia, R. Guarino, N. Pugno, M. Müser, M. Ciavarella, Modeling and simulation in tribology across scales: An overview, Tribol. Int. 125 (2018) 169–199, http://dx.doi.org/10.1016/j.triboint.2018.02.005.

[2] Y. Gao, W. shen Xiao, H. Zhu, Snap-buckling of functionally graded multilayer graphene platelet-reinforced composite curved nanobeams with geometrical imperfections, Eur. J. Mech. A Solids 82 (2020) 103993, http://dx.doi.org/10.1016/j.euromechsol.2020.103993.

[3] V.T. Long, H.V. Tung, Thermal postbuckling behavior of CNT-reinforced composite sandwich plate models resting on elastic foundations with tangentially restrained edges and temperature-dependent properties, J. Thermoplast. Compos. Mater. 33 (10) (2020) 1396–1428, http://dx.doi.org/10.1177/0892705719828789.

[4] S. Maraghechi, J. Hoefnagels, R. Peerlings, O. Rokoš, M. Geers, Experimental full-field analysis of size effects in miniaturized cellular elastomeric metamaterials, Mater. Des. 193 (2020) 108684, http://dx.doi.org/10.1016/j.matdes.2020.108684.

[5] L. Cedolin, et al., Stability of Structures: Elastic, Inelastic, Fracture and Damage Theories, World Scientific, 2010.

[6] B. Orazbayev, N. Kaina, R. Fleury, Chiral waveguides for robust waveguiding at the deep subwavelength scale, Phys. Rev. Appl. 10 (2018) 054069, http://dx.doi.org/10.1103/PhysRevApplied.10.054069.

[7] L. Liu, P. Kamm, F. García-Moreno, J. Banhart, D. Pasini, Elastic and failure response of imperfect three-dimensional metallic lattices: the role of geometric defects induced by selective laser melting, J. Mech. Phys. Solids 107 (2017) 160–184, http://dx.doi.org/10.1016/j.jmps.2017.07.003.

[8] D. Melancon, Z. Bagheri, R. Johnston, L. Liu, M. Tanzer, D. Pasini, Mechanical characterization of structurally porous biomaterials built via additive manufacturing: experiments, predictive models, and design maps for load-bearing bone replacement implants, Acta Biomater. 63 (2017) 350–368, http://dx.doi.org/10.1016/j.actbio.2017.09.013.

[9] J. Arbocz, H. Abramovich, The Initial Imperfection Data Bank at the Delft University of Technology: Part I, Delft University of Technology, 1979.

[10] I. Elishakoff, S.v. Manen, P. Vermeulen, J. Arbocz, First-order second-moment analysis of the buckling of shells with random imperfections, AIAA J. 25 (8) (1987) 1113–1117.

[11] C. Schenk, G. Schuëller, Buckling analysis of cylindrical shells with random geometric imperfections, Int. J. Non-Linear Mech. 38 (7) (2003) 1119–1132, http://dx.doi.org/10.1016/S0020-7462(02)00057-4.

[12] C. Schenk, G. Schuëller, Buckling analysis of cylindrical shells with cutouts including random boundary and geometric imperfections, Comput. Methods Appl. Mech. Engrg. 196 (35–36) (2007) 3424–3434.

[13] M. Broggi, A. Calvi, G.I. Schuëller, Reliability assessment of axially compressed composite cylindrical shells with random imperfections, Int. J. Struct. Stab. Dyn. 11 (02) (2011) 215–236, http://dx.doi.org/10.1142/S0219455411004063.

[14] M. Broggi, G. Schuëller, Efficient modeling of imperfections for buckling analysis of composite cylindrical shells, Eng. Struct. 33 (5) (2011) 1796–1806, http://dx.doi.org/10.1016/j.engstruct.2011.02.019.

[15] J. Kepple, M.T. Herath, G. Pearce, B.G. Prusty, R. Thomson, R. Degenhardt, Stochastic analysis of imperfection sensitive unstiffened composite cylinders using realistic imperfection models, Compos. Struct. 126 (2015) 159–173.

[16] S. Kameshwar, J.E. Padgett, Stochastic modeling of geometric imperfections in aboveground storage tanks for probabilistic buckling capacity estimation, ASCE-ASME J. Risk Uncertain. Eng. Syst. A 2 (2) (2016) C4015005, http://dx.doi.org/10.1061/AJRUA6.0000846.

[17] T.N. Nguyen, S. Lee, P.-C. Nguyen, H. Nguyen-Xuan, J. Lee, Geometrically nonlinear postbuckling behavior of imperfect FG-CNTRC shells under axial compression using isogeometric analysis, Eur. J. Mech. A Solids 84 (2020) 104066, http://dx.doi.org/10.1016/j.euromechsol.2020.104066.

[18] N.D. Duc, P.T. Thang, Nonlinear response of imperfect eccentrically stiffened ceramic–metal–ceramic FGM thin circular cylindrical shells surrounded on elastic foundations and subjected to axial compression, Compos. Struct. 110 (2014) 200–206, http://dx.doi.org/10.1016/j.compstruct.2013.11.015.

[19] V.N.V. Do, C.-H. Lee, Numerical investigation on post-buckling behavior of FGM sandwich plates subjected to in-plane mechanical compression, Ocean Eng. 170 (2018) 20–42, http://dx.doi.org/10.1016/j.oceaneng.2018.10.007.

[20] A.Y. Evkin, O.V. Lykhachova, Design buckling pressure for thin spherical shells: Development and validation, Int. J. Solids Struct. 156–157 (2019) 61–72, http://dx.doi.org/10.1016/j.ijsolstr.2018.06.035.

[21] M. Amir, M. Talha, Imperfection sensitivity in the vibration behavior of functionally graded arches by considering microstructural defects, Proc. Inst. Mech. Eng. C 233 (8) (2019) 2763–2777, http://dx.doi.org/10.1177/0954406218792584.

[22] L. Liu, J.-M. Li, G.A. Kardomateas, Nonlinear vibration of a composite plate to harmonic excitation with initial geometric imperfection in thermal environments, Compos. Struct. 209 (2019) 401–423, http://dx.doi.org/10.1016/j.compstruct.2018.10.101.

[23] S. Turteltaub, G. de Jong, Multiscale modeling of the effect of sub-ply voids on the failure of composite materials, Int. J. Solids Struct. 165 (2019) 63–74, http://dx.doi.org/10.1016/j.ijsolstr.2019.01.031.

[24] H. Shahverdi, M.R. Barati, B. Hakimelahi, Post-buckling analysis of honeycomb core sandwich panels with geometrical imperfection and graphene reinforced nano-composite face sheets, Mater. Res. Express 6 (9) (2019) 095017, http://dx.doi.org/10.1088/2053-1591/ab2b74.

[25] O.M.E.S. Khayal, Literature review on imperfection of composite laminated plates, J. Microsc. Ultrastruct. 5 (3) (2017) 119–122, http://dx.doi.org/10.1016/j.jmau.2017.01.001.
[26] D.D. Nguyen, S.-E. Kim, T.A.T. Vu, A.M. Vu, Vibration and nonlinear dynamic analysis of variable thickness sandwich laminated composite panel in thermal environment, J. Sandw. Struct. Mater. (2020) 1099636219899402, http://dx.doi.org/10.1177/1099636219899402.
[27] A. Stawiarski, M. Chwał, M. Barski, A. Muc, The influence of the manufacturing constraints on the optimal design of laminated conical shells, Compos. Struct. 235 (2020) 111820, http://dx.doi.org/10.1016/j.compstruct.2019.111820.
[28] P. Sidén, A. Eklund, D. Bolin, M. Villani, Fast Bayesian whole-brain fMRI analysis with spatial 3D priors, NeuroImage 146 (2017) 211–225, http://dx.doi.org/10.1016/j.neuroimage.2016.11.040.
[29] T.D. Ngo, A. Kashani, G. Imbalzano, K.T. Nguyen, D. Hui, Additive manufacturing (3D printing): A review of materials, methods, applications and challenges, Composites B 143 (2018) 172–196, http://dx.doi.org/10.1016/j.compositesb.2018.02.012.
[30] M. Shinozuka, G. Deodatis, Simulation of stochastic processes by spectral representation, Appl. Mech. Rev. 44 (4) (1991) 191–204, http://dx.doi.org/10.1115/1.3119501.
[31] M. Grigoriu, On the spectral representation method in simulation, Probab. Eng. Mech. 8 (2) (1993) 75–90, http://dx.doi.org/10.1016/0266-8920(93)90002-D.
[32] C.-C. Li, A. Der Kiureghian, Optimal discretization of random fields, J. Eng. Mech. 119 (6) (1993) 1136–1154, http://dx.doi.org/10.1061/(ASCE)0733-9399(1993)119:6(1136).
[33] W. Betz, I. Papaioannou, D. Straub, Numerical methods for the discretization of random fields by means of the Karhunen-Loève expansion, Comput. Methods Appl. Mech. Engrg. 271 (2014) 109–129, http://dx.doi.org/10.1016/j.cma.2013.12.010.
[34] M. Unser, On the approximation of the discrete Karhunen-Loève transform for stationary processes, Signal Process. 7 (3) (1984) 231–249, http://dx.doi.org/10.1016/0165-1684(84)90002-1.
[35] C.L. Fancourt, J.C. Principe, On the relationship between the Karhunen-Loève transform and the prolate spheroidal wave functions, in: 2000 IEEE International Conference on Acoustics, Speech, and Signal Processing. Proceedings (Cat. No.00CH37100), Vol. 1, 2000, pp. 261–264, http://dx.doi.org/10.1109/ICASSP.2000.861937.
[36] I.G. Graham, F.Y. Kuo, D. Nuyens, R. Scheichl, I.H. Sloan, Analysis of circulant embedding methods for sampling stationary random fields, SIAM J. Numer. Anal. 56 (3) (2018) 1871–1895, http://dx.doi.org/10.1137/17M1149730.
[37] W. Hackbusch, Hierarchical Matrices: Algorithms and Analysis, Vol. 49, Springer, 2015.
[38] A. Lang, J. Potthoff, Fast simulation of Gaussian random fields, Monte Carlo Methods and Applications, 17 (3) (2011) 195–214, http://dx.doi.org/10.1515/mcma.2011.009.
[39] M. Loève, Probability Theory II, in: Graduate Texts in Mathematics, vol. 46, Springer-Verlag, New York, 1978, p. 15.
[40] R.G. Ghanem, P.D. Spanos, Stochastic Finite Elements: A Spectral Approach, Courier Corporation, 2003.
[41] S.P. Huang, S.T. Quek, K.K. Phoon, Convergence study of the truncated Karhunen-Loève expansion for simulation of stochastic processes, Internat. J. Numer. Methods Engrg. 52 (9) (2001) 1029–1043, http://dx.doi.org/10.1002/nme.255.
[42] C. Scarth, S. Adhikari, P.H. Cabral, G.H. Silva, A.P. do Prado, Random field simulation over curved surfaces: Applications to computational structural mechanics, Comput. Methods Appl. Mech. Engrg. 345 (2019) 283–301, http://dx.doi.org/10.1016/j.cma.2018.10.026.
[43] B. Staber, J. Guilleminot, A random field model for anisotropic strain energy functions and its application for uncertainty quantification in vascular mechanics, Comput. Methods Appl. Mech. Engrg. 333 (2018) 94–113, http://dx.doi.org/10.1016/j.cma.2018.01.001.
[44] B. Staber, J. Guilleminot, Stochastic modeling and generation of random fields of elasticity tensors: a unified information-theoretic approach, C. R. Méc. 345 (2017) 399–416, http://dx.doi.org/10.1016/j.crme.2017.05.001.
[45] S. Chu, J. Guilleminot, Stochastic multiscale modeling with random fields of material properties defined on nonconvex domains, Mech. Res. Commun. 97 (2019) 39–45, http://dx.doi.org/10.1016/j.mechrescom.2019.01.008.
[46] A. Stuart, Inverse problems: A Bayesian perspective, Acta Numer. 19 (2010) 451–559.
[47] B. Matern, Spatial Variation, in: Lecture Notes in Statistics, Springer, New York, 1986.
[48] P. Whittle, On stationary processes in the plane, Biometrika 41 (3/4) (1954) 434–449, http://dx.doi.org/10.2307/2332724.
[49] F. Lindgren, H. Rue, J. Lindström, An explicit link between Gaussian fields and Gaussian Markov random fields: the stochastic partial differential equation approach, J. R. Stat. Soc. Ser. B Stat. Methodol. 73 (4) (2011) 423–498, http://dx.doi.org/10.1111/j.1467-9868.2011.00777.x.
[50] G.-A. Fuglstad, F. Lindgren, D. Simpson, H. Rue, Exploring a new class of non-stationary spatial Gaussian random fields with varying local anisotropy, Statist. Sinica 25 (1) (2015) 115–133, http://dx.doi.org/10.2307/24311007.
[51] U. Khristenko, L. Scarabosio, P. Swierczynski, E. Ullmann, B. Wohlmuth, Analysis of boundary effects on PDE-based sampling of Whittle–Matérn random fields, SIAM/ASA J. Uncertain. Quantif. 7 (3) (2019) 948–974, http://dx.doi.org/10.1137/18M1215700.
[52] L. Roininen, J.M.J. Huttunen, S. Lasanen, Whittle-Matérn priors for Bayesian statistical inversion with applications in electrical impedance tomography, Inverse Probl. Imaging 8 (2) (2014) 561–586, http://dx.doi.org/10.3934/ipi.2014.8.561.
[53] L. Roininen, M. Girolami, S. Lasanen, M. Markkanen, Hyperpriors for Matérn fields with applications in Bayesian inversion, Inverse Probl. Imaging 13 (1) (2019) 1–29, http://dx.doi.org/10.3934/ipi.2019001.
[54] M.M. Dunlop, A.M. Stuart, The Bayesian formulation of EIT: Analysis and algorithms, Inverse Probl. Imaging 10 (4) (2016) 1007–1036, http://dx.doi.org/10.3934/ipi.2016030.
[55] P. Sidén, F. Lindgren, D. Bolin, A. Eklund, M. Villani, Spatial 3D Matérn priors for fast whole-brain fMRI analysis, 2019, arXiv arXiv:1906.10591.
[56] A.F. Mejia, Y.R. Yue, D. Bolin, F. Lindgren, M.A. Lindquist, A Bayesian general linear modeling approach to cortical surface fMRI data analysis, J. Amer. Statist. Assoc. 115 (530) (2020) 501–520, http://dx.doi.org/10.1080/01621459.2019.1611582.

[57] D. Bolin, F. Lindgren, Spatial models generated by nested stochastic partial differential equations, with an application to global ozone mapping, Ann. Appl. Stat. 5 (1) (2011) 523–550, http://dx.doi.org/10.1214/10-AOAS383.
[58] J. Guilleminot, A. Asadpoure, M. Tootkaboni, Topology optimization under topologically dependent material uncertainties, Struct. Multidiscip. Optim. 60 (2019) 1283–1287, http://dx.doi.org/10.1007/s00158-019-02247-1.
[59] D. Bolin, K. Kirchner, The rational SPDE approach for Gaussian random fields with general smoothness, J. Comput. Graph. Statist. 29 (2) (2020) 274–285, http://dx.doi.org/10.1080/10618600.2019.1665537.
[60] D. Bolin, J. Wallin, Multivariate type G Matérn stochastic partial differential equation random fields, J. R. Stat. Soc. B 82 (1) (2020) 215–239, http://dx.doi.org/10.1111/rssb.12351.
[61] Y. Daon, G. Stadler, Mitigating the influence of the boundary on PDE-based covariance operators, Inverse Probl. Imaging 12 (5) (2018) 1083–1102, http://dx.doi.org/10.3934/ipi.2018045.
[62] C.A. Rogers, Hausdorff Measures, second ed., Cambridge University Press, 1998.
[63] P. Hansbo, M.G. Larson, Finite element modeling of a linear membrane shell problem using tangential differential calculus, Comput. Methods Appl. Mech. Engrg. 270 (2014) 1–14.
[64] S. Lo, W. Wang, A fast robust algorithm for the intersection of triangulated surfaces, Eng. Comput. 20 (1) (2004) 11–21, http://dx.doi.org/10.1007/s00366-004-0277-3.
[65] S.C. Park, Triangular mesh intersection, Vis. Comput. 20 (7) (2004) 448–456, http://dx.doi.org/10.1007/s00371-004-0251-5.
[66] E.T. Jaynes, Information theory and statistical mechanics, Phys. Rev. 106 (1957) 620–630, http://dx.doi.org/10.1103/PhysRev.106.620.
[67] C.E. Shannon, A mathematical theory of communication, Bell Syst. Tech. J. 27 (3) (1948) 379–423, http://dx.doi.org/10.1002/j.1538-7305.1948.tb01338.x.
[68] C. Geuzaine, J.-F. Remacle, Gmsh: A 3-D finite element mesh generator with built-in pre-and post-processing facilities, Internat. J. Numer. Methods Engrg. 79 (11) (2009) 1309–1331.
[69] R. Ghanem, D. Higdon, H. Owhadi, Handbook of Uncertainty Quantification, Springer, Cham, 2017.
[70] T.-T. Le, J. Guilleminot, C. Soize, Stochastic continuum modeling of random interphases from atomistic simulations. Application to a polymer nanocomposite, Comput. Methods Appl. Mech. Engrg. 303 (2016) 430–449.
[71] X. Wang, M. Jiang, Z. Zhou, J. Gou, D. Hui, 3D printing of polymer matrix composites: A review and prospective, Composites B 110 (2017) 442–458, http://dx.doi.org/10.1016/j.compositesb.2016.11.034.
[72] W. Oropallo, L.A. Piegl, Ten challenges in 3D printing, Eng. Comput. 32 (1) (2016) 135–148, http://dx.doi.org/10.1007/s00366-015-0407-0.
[73] C.N. Kelly, J. Francovich, S. Julmi, D. Safranski, R.E. Guldberg, H.J. Maier, K. Gall, Fatigue behavior of as-built selective laser melted titanium scaffolds with sheet-based gyroid microarchitecture for bone tissue engineering, Acta Biomater. 94 (2019) 610–626, http://dx.doi.org/10.1016/j.actbio.2019.05.046.
[74] L.J. Gomez, A.C. Yücel, L. Hernandez-Garcia, S.F. Taylor, E. Michielssen, Uncertainty quantification in transcranial magnetic stimulation via high-dimensional model representation, IEEE Trans. Biomed. Eng. 62 (1) (2015) 361–372, http://dx.doi.org/10.1109/TBME.2014.2353993.
[75] L. Gomez, F. Cajko, L. Hernandez-Garcia, A. Grbic, E. Michielssen, Numerical analysis and design of single-source multicoil TMS for deep and focused brain stimulation, IEEE Trans. Biomed. Eng. 60 (10) (2013) 2771–2782, http://dx.doi.org/10.1109/TBME.2013.2264632.
[76] A. Opitz, W. Paulus, S. Will, A. Antunes, A. Thielscher, Determinants of the electric field during transcranial direct current stimulation, NeuroImage 109 (2015) 140–150, http://dx.doi.org/10.1016/j.neuroimage.2015.01.033.
[77] B. Fischl, FreeSurfer, NeuroImage 62 (2) (2012) 774–781, http://dx.doi.org/10.1016/j.neuroimage.2012.01.021, 20 YEARS OF fMRI.
[78] W.D. Penny, K.J. Friston, J.T. Ashburner, S.J. Kiebel, T.E. Nichols, Statistical Parametric Mapping: The Analysis of Functional Brain Images, Elsevier, 2011.
[79] O. Puonti, K. Van Leemput, G.B. Saturnino, H.R. Siebner, K.H. Madsen, A. Thielscher, Accurate and robust whole-head segmentation from magnetic resonance images for individualized head modeling, NeuroImage 219 (2020) 117044, http://dx.doi.org/10.1016/j.neuroimage.2020.117044.
[80] R. Dahnke, R.A. Yotter, C. Gaser, Cortical thickness and central surface estimation, NeuroImage 65 (2013) 336–348, http://dx.doi.org/10.1016/j.neuroimage.2012.09.050.
[81] J. Ashburner, K.J. Friston, Unified segmentation, NeuroImage 26 (3) (2005) 839–851, http://dx.doi.org/10.1016/j.neuroimage.2005.02.018.
[82] X. Han, J. Jovicich, D. Salat, A. van der Kouwe, B. Quinn, S. Czanner, E. Busa, J. Pacheco, M. Albert, R. Killiany, P. Maguire, D. Rosas, N. Makris, A. Dale, B. Dickerson, B. Fischl, Reliability of MRI-derived measurements of human cerebral cortical thickness: The effects of field strength, scanner upgrade and manufacturer, NeuroImage 32 (1) (2006) 180–194, http://dx.doi.org/10.1016/j.neuroimage.2006.02.051.
[83] B. Fischl, A.M. Dale, Measuring the thickness of the human cerebral cortex from magnetic resonance images, Proc. Natl. Acad. Sci. 97 (20) (2000) 11050–11055, http://dx.doi.org/10.1073/pnas.200033797.
[84] H.D. Rosas, A.K. Liu, S. Hersch, M. Glessner, R.J. Ferrante, D.H. Salat, A. van der Kouwe, B.G. Jenkins, A.M. Dale, B. Fischl, Regional and progressive thinning of the cortical ribbon in Huntington's disease, Neurology 58 (5) (2002) 695–701, http://dx.doi.org/10.1212/WNL.58.5.695.
[85] K. Crane, C. Weischedel, M. Wardetzky, The heat method for distance computation, Commun. ACM 60 (11) (2017) 90–99, http://dx.doi.org/10.1145/3131280.
[86] S.N. Makarov, G.M. Noetscher, T. Raij, A. Nummenmaa, A quasi-static boundary element approach with fast multipole acceleration for high-resolution bioelectromagnetic models, IEEE Trans. Biomed. Eng. 65 (12) (2018) 2675–2683, http://dx.doi.org/10.1109/TBME.2018.2813261.
[87] L. Gomez, TMS E-field solvers, 2019, URL https://github.com/luisgo/TMS_Efield_Solvers.